Chemical, Structural, and Electronic Aspects of Formation and Degradation Behavior on Different Length Scales of Ni-Rich NCM and Li-Rich HE-NCM Cathode Materials in Li-Ion Batteries

Lea de Biasi, Björn Schwarz, Torsten Brezesinski, Pascal Hartmann, Jürgen Janek,* and Helmut Ehrenberg*

In order to satisfy the energy demands of the electromobility market, both Ni-rich and Li-rich layered oxides of NCM type are receiving much attention as high-energy-density cathode materials for application in Li-ion batteries. However, due to different stability issues, their longevity is limited. During formation and continuous cycling, especially the electronic and crystal structure suffers from various changes, eventually leading to fatigue and mechanical degradation. In recent years, comprehensive battery research has been conducted at Karlsruhe Institute of Technology, mainly aiming at better understanding the primary degradation processes occurring in these layered transition metal oxides. The characteristic process of formation and mechanisms of fatigue are fundamentally characterized and the effect of chemical composition on cell chemistry, electrochemistry, and cycling stability is addressed on different length scales by use of state-of-the-art analytical techniques, ranging from "standard" characterization tools to combinations of advanced in situ and operando methods. Here, the results are presented and discussed within a broader scientific context.

1. Introduction

Layered transition metal oxides are widely used as positive electrode materials for rechargeable Li-ion batteries (LIBs). For reaching the ambitious goals in the electric vehicle and large-scale energy storage sectors, sustainable and environmentally friendly solutions providing higher energy density and lower costs are required. Current state-of-the-art LIBs using, e.g., well-established $LiNi_{1/3}Co_{1/3}Mn_{1/3}O_2$ (NCM111) cathode material are yet not able to fulfill all these demands. In order to increase the energy density of LIBs, battery producers and researchers pursue various strategies. Substitution of expensive Co by Ni to achieve $LiNi_{1-x-y}Co_xMn_yO_2$ compounds with $x < 0.3$ in order to increase the structural stability at high state-of-charge (SOC) is one possible approach. Another promising material class is represented by Li-rich high-energy NCM (HE-NCM) materials (cLi$_2$MnO$_3$·[1 − c]LiTMO$_2$ [TM = Ni, Co, Mn, etc.]). All of these subgroups of layered oxides have in common a crystal structure that is prone to irreversible changes and fatigue during continuous Li (de-)intercalation. The relevant changes in electronic and crystal structure strongly depend on the particular cathode composition and micro/nano-structure. The development of a target-oriented roadmap to improved LIBs that meet the above requirements must address the underlying mechanisms on different cell levels, i.e., from the atomic level to the electrode level. A comprehensive summary of the properties and developments in the field of Ni-rich NCM[1–9] and Li-rich HE-NCM[10–16] has been presented recently

Dr. L. de Biasi, Dr. B. Schwarz, Prof. H. Ehrenberg
Institute for Applied Materials-Energy Storage Systems (IAM-ESS)
Karlsruhe Institute of Technology (KIT)
Hermann-von-Helmholtz-Platz 1
76344 Eggenstein-Leopoldshafen, Germany
E-mail: helmut.ehrenberg@kit.edu

Dr. L. de Biasi, Dr. T. Brezesinski, Dr. P. Hartmann, Prof. J. Janek
Battery and Electrochemistry Laboratory (BELLA)
Institute of Nanotechnology (INT)
Karlsruhe Institute of Technology (KIT)
Hermann-von-Helmholtz-Platz 1
76344 Eggenstein-Leopoldshafen, Germany
E-mail: juergen.janek@kit.edu

Dr. P. Hartmann
BASF SE
Carl-Bosch-Straße 38, 67056 Ludwigshafen, Germany

Prof. J. Janek
Institute of Physical Chemistry and Center for Materials Research
Justus-Liebig-University Giessen
Heinrich-Buff-Ring 17, 35392 Giessen, Germany

by several authors. Here, we focus on the detailed characterization of these materials on different length scales, including the processes during formation and fatigue.

After a brief introduction of the different materials addressed here, their characteristic process of formation and mechanisms of fatigue are discussed with respect to cell chemistry, electrochemistry, and cycling stability. Based on the fundamental results of our experimental studies on the material level, the effect of formation and fatigue on different cell levels is evaluated within a broader scientific context.

1.1. Ni-Rich NCM and NCA

A large number of layered lithium transition metal oxides are described by the general formula $LiTMO_2$ (TM = Ni, Co, Mn, Al, etc.) and crystallize in a rhombohedral $R\overline{3}m$ structure,[11,17,18] derived from the cation-ordered rock-salt superstructure (as for α-$NaFeO_2$).[19,20] Since the commercialization of LIBs in 1991, the Co-rich endmember $LiCoO_2$ (LCO) is probably the most widely used cathode active material (CAM). However, its practical capacity is limited to around 140 mAh g^{-1} at the upper cutoff voltage (COV) of 4.3 V vs Li$^+$/Li.[21–25] During the 1990s, also the Ni-rich endmember $LiNiO_2$ (LNO) was considered an interesting CAM for future battery applications,[26,27] as it offers higher practical capacity and lower costs compared to LCO. However, a stable and wide compositional range, especially with respect to Li content, is a prerequisite to maximize the capacity, energy and cycle life of an electrode material. Unfortunately, different structural and chemical stability issues did not allow the use of LNO in any real-world application. Better stability is achieved when Ni is partially substituted by other metals (mainly Mn, Co, and Al). Today, the so-called NCA ($LiNi_{1-x-y}Co_xAl_yO_2$) and NCM ($LiNi_{1-x-y}Co_xMn_yO_2$) materials make up some of the most frequently used CAMs in LIBs, as their stability benefits from the synergetic effect of the different metals. The state-of-the-art CAM $LiNi_{0.6}Co_{0.2}Mn_{0.2}O_2$ (NCM622) delivers a specific capacity of more than 170 mAh g^{-1} in the voltage range between 3.0 and 4.3 V vs Li$^+$/Li. However, because of the increasing demand in energy density, the general composition is pushed more and more toward Ni-rich materials. Ni-rich NCM (Ni content >> 1/3) allows for higher degrees of delithiation due to two-electron transfer via Ni^{2+}/Ni^{3+} and Ni^{3+}/Ni^{4+}, thus enabling specific capacities in excess of 190 mAh g^{-1}. Unfortunately, in particular high-Ni NCM CAMs suffer from severe capacity fading and degradation, which is believed to be associated with structural changes during cycling (contraction of c-axis and unit cell volume with delithiation and collapse of Li–O layers at high SOC).[17,28] These structural changes cause fracture and mechanical degradation of CAM particles, leading to formation of new reactive surfaces and cell impedance rise.[29]

1.2. Li-Rich HE-NCM

Cation or anion substitution is a common way to achieve stabilization of transition metal oxide host structures, as described for $LiNi_{1-x}Co_xO_2$ (LNCO) with Al^{3+} substitution (see above).[30,31] An alternative approach to improve structural stability and electrochemical performance is to use structural units as

Lea de Biasi is currently working at the Battery Technical Center at Karlsruhe Institute of Technology (KIT). She obtained her B.Sc. degree from University of Freiburg and M.Sc. degree from LMU Munich in 2010 and 2012, respectively. She completed her Ph.D. degree at KIT in 2016, and then joined the Battery and Electrochemistry Laboratory (BELLA), a joint KIT/BASF SE laboratory, as a postdoctoral fellow. Her research interests encompass the structural and electrochemical characterization of next-generation electrode materials as well as the investigation into new cell designs and development of advanced lithium-ion batteries.

Björn Schwarz received his Ph.D. degree in materials science from Technische Universität Darmstadt in 2007. He then worked as a postdoctoral fellow (2007–2012) at the Leibniz Institute for Solid State and Materials Research Dresden, with main research activities on physical/magnetic characterization of transition metal oxides and phase-separated metallic glasses. Since 2012, he has been senior scientist at the Institute for Applied Materials–Energy Storage Systems at Karlsruhe Institute of Technology (KIT). His current research interests include the relation between atomic/electronic structure and physical properties/electrochemical reaction mechanisms in various kinds of energy-storage materials.

substitutional elements rather than cations or anions.[32–34] "Layered–layered" two-phase materials as a kind of composite of Li_2MnO_3[34–39] and $LiTMO_2$ (TM = Ni, Co, Mn), formally written as $cLi_2MnO_3\cdot[1 - c]LiTMO_2$ and commonly referred to as Li-rich layered oxides, are considered promising electrode materials with superior Li-storage and thermal properties over conventional layered materials.[40–42] While NCA and NCM CAMs practically offer specific capacities around 200 mAh g^{-1}[43–47] due to their limited stability range for Li extraction, the class of Li-rich layered materials is capable of delivering specific capacities >250 mAh g^{-1}.[15,48–53]

1.3. Degradation and Material Fatigue

In recent years, significant effort has been made to better understand the mechanisms leading to capacity fading, gassing, and
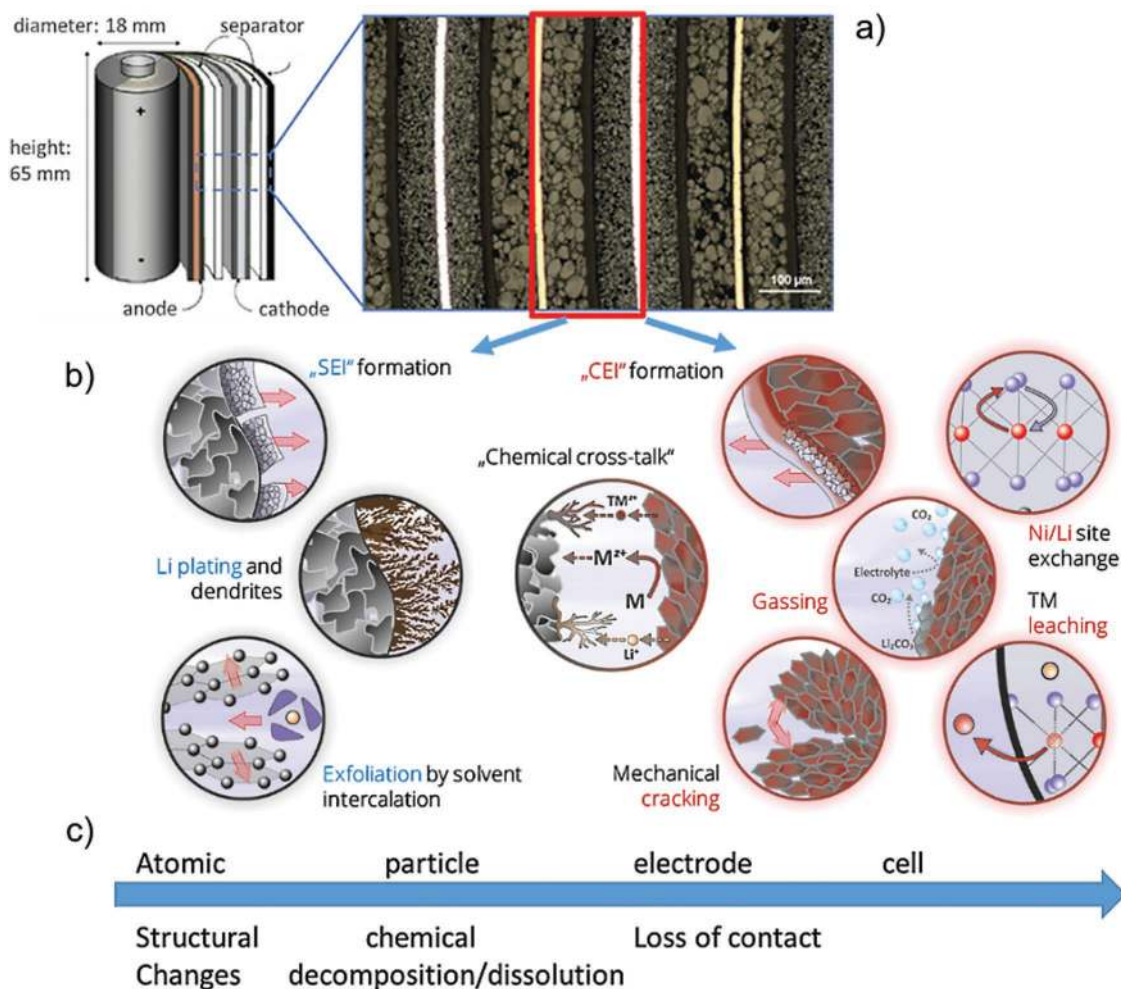
1900985 (2 of 24)

**ADVANCED
SCIENCE NEWS**

www.advancedsciencenews.com

**ADVANCED
MATERIALS**

www.advmat.de

Figure 1. Degradation scheme of LIB cells using Ni-rich NCM and Li-rich HE-NCM CAMs. a) Schematic figure of a practical battery cell and cross-sectional image of the corresponding electrode layers. Adapted with permission.[89] Copyright 2012, Carl Hanser Verlag GmbH & Co.KG, München. b,c) Degradation processes and side reactions occurring on different length scales.

impedance rise in cells using Ni-rich NCM[28,29,54–63] and Li-rich HE-NCM CAMs.[37,38,45,49,50,64–82] Various processes have been identified to cause degradation of electrode materials, thereby limiting the overall cell performance and its longevity.[83–86] The term "aging" refers to the calendar degradation of a material or a full-cell, i.e., the degradation under static conditions, for example during storage at ambient or elevated temperature and at constant SOC.[87,88] The term "material fatigue" denotes the degradation of a material as a result of its repetitive use, i.e., in case of LIB electrode materials, the continuous insertion and extraction of Li ions into and from the host structure, respectively. Here, we focus on aspects of material fatigue (rather than aging) of Ni-rich NCMs and Li-rich HE-NCMs and how fatigue, in general, affects the cell degradation.

An overview of the most critical degradation mechanisms on different levels of the electrochemical cell is given in **Figure 1**. The material fatigue of layered transition metal oxides is commonly the result of correlated changes in electronic and structural properties. Apart from structural changes on the atomic level (including phase transformations), especially the volume contraction/expansion during continuous Li (de-)intercalation

can lead to disintegration and contact loss between the CAM particles, the conductive carbon black additive, and the current collector. This, in turn, can lead to accumulation of local microstructural changes and eventually to mechanical failure.[90,91] As a result, cracks form and propagate through the secondary particles, resulting in loss of connectivity within the electrode. Note that for future applications in all-solid-state battery cells, where the volume cannot expand into a liquid electrolyte reservoir, the consequences of volume changes are even more critical.[92] In general, Ni-rich NCM CAMs suffer from larger volumetric changes with delithiation than low-Ni compounds. Hence, depending on the Ni content, mechanical failure may become a severe problem.[28] Another issue of NCM CAMs, especially Ni-rich ones, is their relatively high surface reactivity (already during storage at ambient conditions).[93] Because of particle fracture, an increasing fraction of fresh surface is continuously exposed to the electrolyte. This results in progressive surface film formation—comparable to solid electrolyte interphase (SEI) formation at the anode side—accompanied by capacity fading due to irreversible loss of mobile Li and increase in cell impedance.[94] An additional issue that may arise when layered lithium transition metal

**ADVANCED
SCIENCE NEWS**
www.advancedsciencenews.com

**ADVANCED
MATERIALS**
www.advmat.de

oxides are used as the CAM is the dissolution of TM ions, triggered by surface reactions with hydrofluoric (HF) acid, and their migration and incorporation into the graphite SEI.[95–99] Another consequence is gas evolution due to electrolyte decomposition, raising safety issues. In summary, all of the aforementioned processes contribute to the capacity and power decay of NCM-based LIBs, and therefore require profound understanding.

1.4. Characterization Strategies

Depending on the relevant length scale of the specific degradation process/mechanism (Figure 1), different analytical tools are required. Operando techniques are most suitable to study the chemical activity and structural transformations under real battery cell conditions during electrochemical cycling. Diffraction experiments, such as X-ray (XRD) and neutron diffraction (ND), provide bulk-representative "global" information about the phase constitution, space group symmetry, lattice parameter(s), real structure parameters (crystallographic size and strain), and space-averaged atomic structure (crystallographic site occupation). X-ray absorption spectroscopy (XAS) provides local information (element specific oxidation states [electronic structure] and atomic coordination), and therefore represents a powerful tool to gain insights into the correlation of crystallographic and electronic structure changes. Changes in the underlying primary crystal structure will directly translate into changes on the length scale of secondary particles, e.g., irreversible phase transformations with formation of microcracks and pulverization of the active material as result of crystallographic strain and lattice mismatch between adjacent domains. Moreover, side reactions of the electrode with the electrolyte may lead to further modification of the surface. Electron microscopy, such as scanning electron (SEM) and transmission electron microscopy (TEM), are well suited for the post mortem analysis of such processes. Typically, side reactions involve the evolution of gas, particularly at high SOC, e.g., when electrolyte is decomposed due to oxidation reactions at the cathode[56,100] or when oxygen is released from the crystal lattice of the CAM.[80,101] In a closed cell compartment, this will lead to an increase in internal pressure and, in the worst case, to bursting of the cell housing. Another factor affecting both stress and strain are volume changes of electrode particles due to variations in lattice parameters depending on the Li content. In situ pressure analysis is a feasible tool to detect such volume changes by monitoring the pressure evolution with cycling operation. Overall, this method can be used to study the effect of changes in unit cell volume of single electrode particles (projected onto the electrode level).[102,103] Differential electrochemical mass spectrometry (DEMS) lends itself for thorough analysis of the evolved gaseous species and their quantification. Of note, isotopic labeling even allows determination of specific reaction pathways, leading to the release of gas.[101]

2. Crystal and Electronic Structure

2.1. Structure of Ni-Rich NCM

Layered NCMs or, in general, $LiTMO_2$ compounds crystallize in a rhombohedral $R\bar{3}m$ structure,[17,18,104] which can be derived from the ordered rock-salt structure of α-$NaFeO_2$[19,20] (**Figure 2**a). Oxygen atoms form a cubic close-packed (ccp) lattice with rhombohedral distortion along the c-direction, resulting in layers formed by edge-sharing octahedra. The octahedral sites of the somewhat thinner layer (Wyckoff position 3a) are occupied mainly by transition metals (TM layer), whereas those of the somewhat thicker layer (Wyckoff position 3b) are occupied mainly by lithium (Li layer), yielding $[Li]_{3b}[TM]_{3a}[O_2]_{6c}$.[105] Especially in the presence of manganese, the materials tend to Li excess, meaning that a small fraction of the 3a sites is occupied by Li ions, too. Hence, NCM is frequently denoted as $Li_{1+z}(Ni_{1-x-y}Co_xMn_y)_{1-z}O_2$. By contrast, LNO tends to Li deficiency, meaning that nickel occupies some of the 3b sites. In the discussion of $LiTMO_2$ CAMs, this type of structure is often referred to as H1-type structure (mainly in the context of LNO with reference to the hexagonal structure of pristine material)[26,106] or O3-type structure (with reference to the three-fold stacking sequence of TMO_2 layers that is needed to describe the unit cell).[10,107] The TM site can be occupied by a combination of Ni, Co, and Mn as well as by some other metal ions, such as Al in the NCA case. Some Li/TM disorder between the 3b and 3a crystallographic sites (up to several
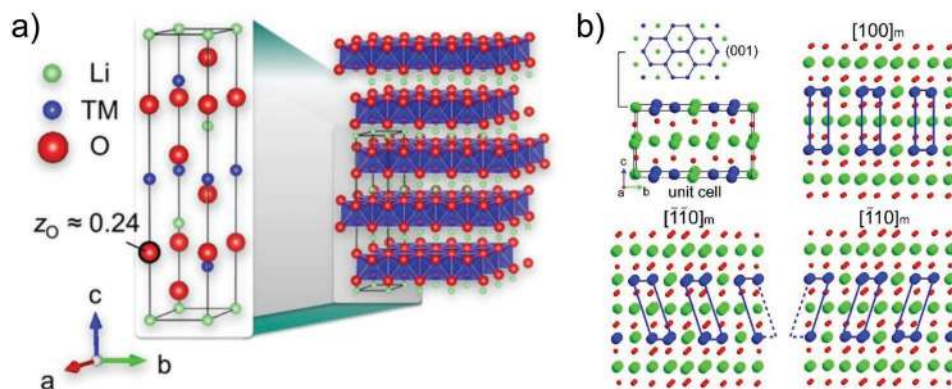

Figure 2. a) Layered crystal structure of NCM. Reproduced with permission.[61] Copyright 2017, American Chemical Society. b) Layered crystal structure of Li_2MnO_3 with $C2/m$ space group symmetry. $[100]_m$, $[-1-10]_m$, and $[-110]_m$ crystallographic orientations with transition metal and Li columns within the TM layer aligned along the projection direction.

atomic percent) is commonly observed for this class of materials and known to affect the electrochemical properties. However, the $R\overline{3}m$ space group symmetry remains unaffected by this type of disorder. According to literature reports, even the individual TM species (Mn, Ni, and Co) may exhibit long-range ordering in the TM layer, leading to symmetry reduction and appearance of superstructure reflections in selected-area electron diffraction (SAED) patterns. Note that SAED is more sensitive to slight differences in electron density than is XRD.[108]

2.2. Structure of Li-Rich HE-NCM

Li-rich HE-NCM CAMs can be seen as so-called "layered–layered" two-phase materials (it is an open discussion whether they should be described as single-phase solid solution or two-phase nanodomain materials), as they comprise a kind of composite of Li_2MnO_3[35–39] and $LiTMO_2$ (TM = Ni, Co, Mn), formally written as $cLi_2MnO_3\cdot[1-c]LiTMO_2$. Commonly used layered $LiTMO_2$[109–111] and spinel $LiTM_2O_4$ compounds (TM = Mn, Ni, and Co; Mg and/or Al for stabilization) share a ccp oxygen framework (rhombohedrally distorted for $LiTMO_2$) with the same interlayer distance of about 4.7 Å. $Li_2TM'O_3$ (TM' = Mn, Ti, Zr)[112] as an electrochemically inactive compound also exhibits a ccp oxygen lattice with very similar lattice parameters but $C2/m$ symmetry (Figure 2b). It is supposed to enhance the structural stability when embedded as building blocks in either the $LiTMO_2$ or $LiTM_2O_4$ host matrix.[113] Hence, the composite nanostructure of HE-NCM can be considered to consist of a $R\overline{3}m$ NCM host matrix with coherently embedded Li_2MnO_3-like domains of $C2/m$ symmetry. Because of the lowered space group symmetry of Li_2MnO_3-like domains, the oxygen framework is slightly distorted compared to that of the $R\overline{3}m$ matrix, but still there exists a coherent interconnecting ccp oxygen lattice for the entire heterostructured material (crystal lattice). Even though the rhombohedral NCM matrix and the monoclinic Li_2MnO_3-like domains have different space group symmetries, their structures are very similar and can hardly be distinguished from each other at first glance using TEM or XRD. The most significant difference between these two structures is related to the Li/Mn honeycomb ordering within the TM layers of the Li_2MnO_3-like domains. This intersects the Mn atom sequence in the TM layer with a Li atom after every two Mn atoms when projected along the $[-1-10]_m$, $[-110]_m$ or $[100]_m$ crystallographic orientations, corresponding to 120° rotations around an axis perpendicular to the layers ($[103]_m$). These three orientations can be described equivalently as a layer stacking sequence with different in-layer translational shifts from TM layer to TM layer: the projected Li atom columns are stacked directly above each other or they are tilted toward one or the other side (Figure 2b). By choosing a specific crystal orientation for the rhombohedral NCM host matrix that coincides with either the $[-1-10]_m$, $[-110]_m$ or $[100]_m$ orientation of the embedded $C2/m$ domains, it is possible to distinguish both types of composite constituents, namely the NCM and Li_2MnO_3-like domains, in HRTEM images. While the $R\overline{3}m$ NCM host matrix shows a solid line contrast, representing the TM within the TM layer, the Li_2MnO_3-like domains are indicated by a dot-like contrast due to the Li intersected TM layers. Furthermore, the Li_2MnO_3 stacking faults can be observed whenever the sequence changes the stacking "direction," e.g.,

from $[100]_m$ to $[-110]_m$. The nanostructure of a "layered–layered" composite can therefore be characterized by the dimensions of the Li_2MnO_3-like domains and further by the density of stacking faults therein (the number of subsequent lattice layers without any stacking fault). The SAED pattern of a so-aligned pristine Li-rich layered oxide crystallite shows $C2/m$-related superstructure reflections that are broadened depending on the domain sizes and stacking fault density. By selecting these $C2/m$-related reflections for dark-field imaging, it is possible to gain information about the lateral (projected) distribution of Li_2MnO_3-like domains. The most pronounced $C2/m$-related superstructure reflections 020, 110, −111, 021, and 111 at low scattering angles of synchrotron-based diffraction patterns can be fitted using the DIFFaX program,[114] particularly designed to account for planar defects in crystal structures.

Here, the fitting procedure is used to estimate the number of defect-free stacked TM layers with Li_2MnO_3 configuration and in-plane lateral domain dimensions to complete the information from HRTEM studies by a complementary bulk-sensitive diffraction method. Note that by this evaluation method, the number of subsequently stacked defect-free TM layers is determined. The Li_2MnO_3 domains that are observed by HRTEM or dark-field TEM imaging might have larger dimensions, since they are considered simply as coherent domains of Li_2MnO_3 character without subdivision into defect-free blocks. For more detailed information on the pristine structures of both NCM[2,17,18,28,61,115,116] and HE-NCM,[34,41,48,51,112,117–125] we refer to other reports available in the literature.

2.3. Thermal Stability of NCM

The electrochemical properties and the structural and thermal stability of NCM CAMs strongly depend on their composition, as demonstrated for example by Noh et al.[18] In particular, the Ni content is a critical parameter determining the thermal stability[53] as well as the magnitude of changes in the crystal structure upon delithiation.[18,28,61] As for practical applications of Ni-rich NCMs, the thermal stability plays an important role, as it directly affects the LIB safety. Especially Ni-rich NCMs at high SOC are subjected to spontaneous reduction of Ni^{4+} to Ni^{2+} during heating, accompanied by release of oxygen.[18,31,53,111,126–128] Systematic comparisons demonstrated that the higher the Ni content in the NCM CAM, the lower the onset temperature of the decomposition reaction.[18,53]

2.4. Crystallographic Changes in NCM

Besides thermal shortcomings, the changes in crystal structure during cycling constitute another major problem, impeding the practical use of Ni-rich NCM CAMs. Crystallographic volume changes and multiphase transformations are assumed to be responsible for the capacity fading and to be one of the main factors governing the material fatigue.[129] Operando XRD is well suited to analyze crystallographic changes under dynamic conditions, for example during electrochemical cycling, and several studies have reported on the lattice parameter changes of NCM CAMs with cycling,[17,18,53,61,63,104,129–134] but only few of them
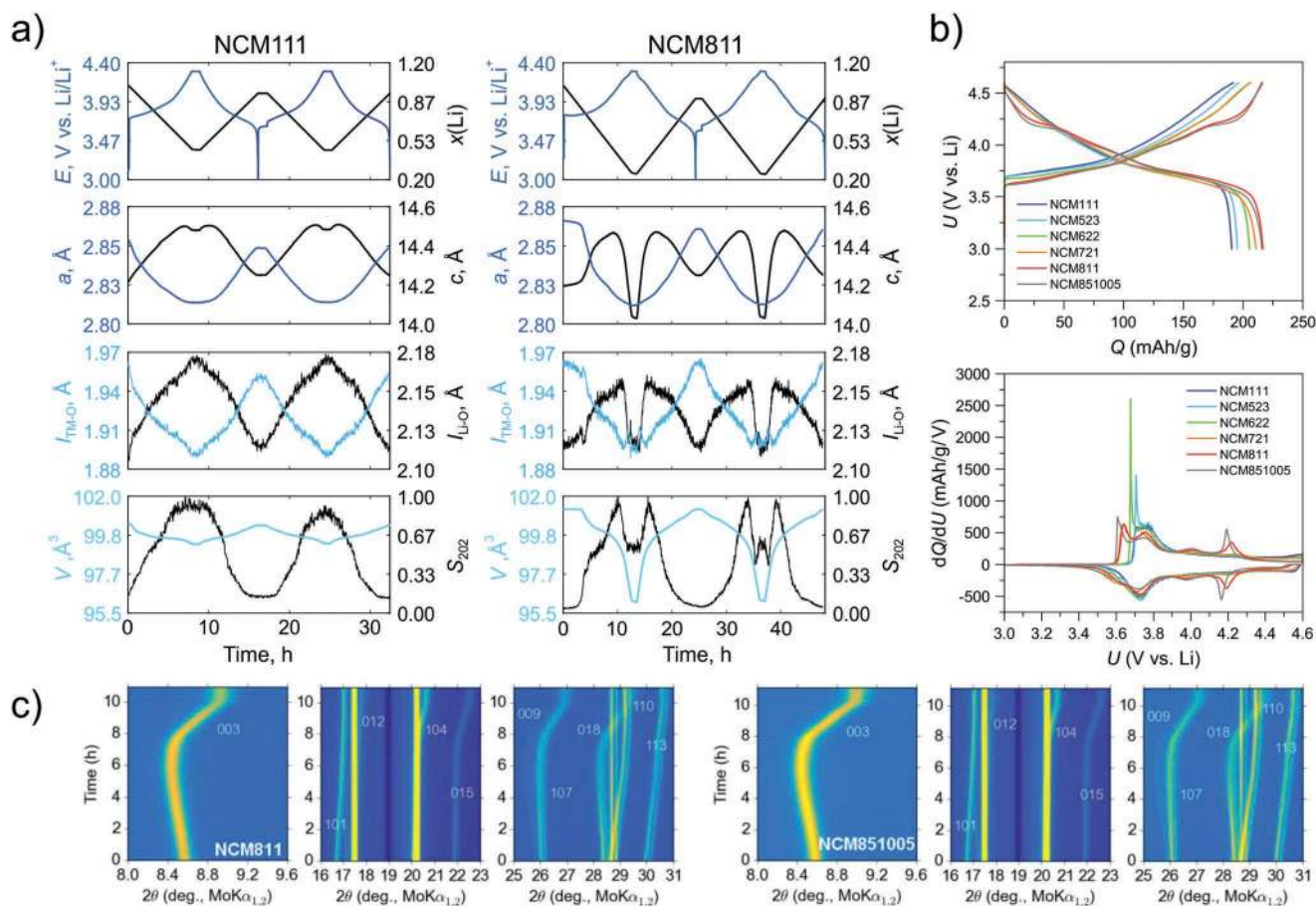
Figure 3. a) Structural refinement results for NCM111 and NCM811 (cell voltage E, lattice parameters a and c, TM–oxygen bond length $l_{TM–O}$, lithium–oxygen bond length $l_{Li–O}$, unit cell volume V, and anisotropic microstrain parameter S_{202}). The lithium content $x(Li)$ was calculated from the electrochemical data. Reproduced with permission.[28] Copyright 2017, American Chemical Society. b) Charge/discharge curves (top) and the corresponding differential capacity curves (bottom) of different low-, medium-, and high-Ni NCM CAMs. c) Contour plots of operando XRD patterns for selected 2θ ranges obtained on NCM811- and NCM851005-based cells during the charge cycle (delithiation). b,c) Adapted with permission.[61] Copyright 2017, American Chemical Society.

revealed sufficient time and angular resolutions. Hence, some of our studies aimed at analyzing the changes in the NCM crystal structure during Li (de-)intercalation under realistic conditions.[28,61,62] For this purpose, an advanced laboratory XRD setup was used, specially dedicated for battery research at Karlsruhe Institute of Technology (KIT).[135] The high-flux beam (Mo K$\alpha_{1,2}$) and the fast 2D detector of the setup allowed performing operando XRD experiments with good time resolution and tracking crystallographic parameters, such as unit cell volume, atomic positions, and crystallographic strain, directly as a function of Li content in the electrode. **Figure 3**a depicts results from Kondrakov et al.,[28] showing the crystallographic changes during charge and discharge of low-Ni (NCM111) and high-Ni NCM (NCM811, 80% Ni). The corresponding diffraction patterns were acquired with a time resolution of 150 s, being equivalent to $\Delta x(Li) \approx 0.003$ per pattern. Recent studies have shown that the lattice parameters are subjected to SOC-dependent nonmonotonic changes.[61,104] In particular, at high SOC, the overall lattice parameter changes are highly anisotropic. The a lattice parameter in both NCM111 and NCM811 CAMs gradually decreases in a similar manner (Figure 3a). However, the absolute change in the a-axis is larger for NCM811, which can be attributed

to a higher specific capacity (189 mAh g^{-1} for NCM811 vs 149 mAh g^{-1} for NCM111), i.e., higher degree of delithiation at the upper COV of 4.3 V (vs Li$^+$/Li). Even more pronounced composition-dependent differences are seen in the behavior of the c-axis. Ultimately, the variations in the c lattice parameter are the result of changes in both the TM–oxygen bond length $l_{TM–O}$ and the Li–oxygen bond length $l_{Li–O}$. In the case of NCM111, the bond lengths reveal an inverse and almost linear behavior, whereas it is much more complex for NCM811. This difference is also reflected in the c lattice parameter. In the case of NCM111, it virtually only increases (a slight decrease was observed at $x(Li) = 0.5$ until the end of charge). In contrast, the c lattice parameter of NCM811 increases at first, too, but dramatically decreases as soon as the Li content is ≤0.5. These results demonstrate clearly that NCM811 undergoes more pronounced structural changes than NCM111. A similar trend in lattice parameters was seen for a variety of NCM CAMs, with clear indications of larger changes with increasing Ni content.[17,18,61,63,104,130–133] An illustration/structural description of the NCM lattice with delithiation is given by Lee et al.[136] Overall, this indicates the stress that NCM CAMs experience when the Ni content is increased (and with that the specific

ADVANCED
SCIENCE NEWS
www.advancedsciencenews.com

ADVANCED
MATERIALS
www.advmat.de

capacity for a given voltage range; Figure 3b). A better understanding of the structural mechanisms in Ni-rich NCM can be achieved by taking LNO as a model system. In the case of LNO, the structure undergoes various phase transformations during charging. At least four phases are described in the literature, i.e., the hexagonal H1, the monoclinic M, the hexagonal H2, and the hexagonal H3 phases, appearing in the same order upon delithiation.[26,27,106,137–139] A detailed description and visualization of the LNO structure is provided in a recent review article.[140] Li et al.[139] recently presented results from operando XRD on LNO. Here, the crystallographic changes are so distinct that the appearance of individual Li_xNiO_2 phases can be readily tracked. Apparently, especially the H2–H3 transformation is accompanied by a strong discontinuous shrinkage of the c lattice parameter.

Although the evolution of lattice parameters suggests solid solution behavior at first glance, the presence of a multistep phase transformation mechanism similar to that observed for LNO cannot be ruled out. If the lattice differences between individual phases were marginally small, the peak splitting would not be large enough to be seen and the reflections would only broaden. In fact, an increase in full width at half-maximum (FWHM) of several Bragg reflections was observed for some NCM CAMs[28,61] in different Li concentration regimes, correlating well with the monoclinic phase and H2–H3 coexistence regions (see contour plots of NCM811 and NCM851005 [85% Ni] in Figure 3c).

A suitable way of identifying electrochemically induced two-phase transformations is via examination of the charge/discharge curves, given that phase coexistence regions are indicated by minimum slopes (plateaus) in the cell potential. In Li_xNiO_2, the different phase regions can be clearly observed in the voltage profile.[27,137,139,141,142] As can be seen in Figure 3b, the charge/discharge curves as well as the differential capacity curves of low- and medium-Ni NCM CAMs only show features characteristic of the monoclinic phase region.[61] However, the voltage curves of high-Ni (≥80%) NCMs reveal an additional plateau at around 4.15 V (vs Li^+/Li).[28,61–63,130,143–147] Comparison of the differential capacity (dQ/dU) with differentials of the c lattice parameter [dc/dU and dc/dx(Li)] and unit cell volume revealed clear correlations, thus providing evidence of the existence of the H2–H3 transformation in the case of $LiNi_{0.8}Co_{0.1}Mn_{0.1}O_2$[61,62] and $LiNi_{0.85}Co_{0.1}Mn_{0.05}O_2$,[61] in agreement with observations on both $LiNi_{0.9}Co_{0.05}Mn_{0.05}O_2$ and $LiNi_{0.95}Co_{0.025}Mn_{0.025}O_2$ by Ryu et al.[144] They detected a peak broadening of the 003 reflection, which was ascribed to the coexistence of both phases at the end of charge. Interestingly, the H2–H3 signal is not present in the voltage profile of NCA (85% Ni), thereby hinting at the stabilizing role of Al.[88] While the c-axis of NCA also experiences considerable shrinkage at high degrees of delithiation (high SOC), it does not seem to be discontinuous and the material exhibits solid solution properties similar to low- and medium-Ni NCMs.

Because of the severe volume change, the H2–H3 transformation is believed to have the most significant effect of all phase transformations on the intrinsic material stability. Ryu et al.[144] tested several Ni-rich NCM CAMs (with Ni fractions of 0.6, 0.8, 0.9, and 0.95) to characterize their degradation behavior. They found that the capacity fading is predominantly caused by gradual surface degradation when the Ni content is

below 80%. NCM CAMs with ≥80% Ni, however, appeared to mostly degrade due to the anisotropic shrinkage during the H2–H3 phase transition. Hence, it is of utmost importance to better understand the origin of processes that ultimately govern the changes in crystal structure.

For quite some time, the evolution of lattice parameters of layered $LiTMO_2$ compounds, and especially the collapse of the c-axis at high SOC, was not well understood and treated only in few theoretical[148] and experimental[28,149,150] studies. The a lattice parameter is assumed to reflect the TM–TM distance (within the TM layer). When the ionic radii of TMs (mainly Ni) decrease with increasing oxidation state, the a lattice parameter decreases. The c lattice parameter is closely linked to the interslab distance of the Li layers. The initial increase in c is usually interpreted as a result of increasing Coulomb repulsion with progressive Li extraction, since Li is expected to effectively screen the electrostatic repulsion between the oxygen layers. The screening effect is reduced at relatively higher SOC, resulting in increased repulsion and expansion along the c-axis. So far, the reason for the sudden contraction of the interslab distance, leading to the decrease in lattice parameter, particularly in Ni-rich NCMs, has not been explained in full. To shed more light on the charge evolution, density functional theory (DFT) calculations have been performed by Kondrakov et al.[62] for the model system Li_xNiO_2. Based on experimental XRD results obtained on NCM811, the Li content was varied in the range x(Li) = 1.0–0.25 and the changes in crystal structure were calculated. The nonmonotonic behavior of the lattice along the c-axis, i.e., the changes in c lattice parameter with decreasing lithium content, could be well reproduced by the calculations. The average Bader charges for nickel and oxygen were determined, too. The main results can be described as follows: i) nonmonotonic change in Ni charge, i.e., at first, an increase, followed by a break of the positive trend when x(Li) < 0.5 (the Ni charge slightly decreases between 0.5 > x(Li) > 0.25) and ii) O charge increases during delithiation, with the total change being largest when x(Li) decreases from 0.5 to 0.25. In conclusion, these data suggest charge transfer from oxygen to nickel at high SOC. Furthermore, large mixing between the 2p orbitals of oxygen and the partially filled e_g orbitals of nickel was observed by soft XAS. The contribution of nickel to the charge compensation was confirmed by changes in spectra of the Ni K- and L-edges.[62] Hence, the results provide an explanation for the charge-induced shrinkage of the TM–oxygen layer, as seen by operando XRD for NCM811 (Figure 3a). In addition, they demonstrate the correlation between the collapse of the layered structure (i.e., the Li–oxygen layer) and charge transfer, the latter of which results in partial oxidation of oxygen. Using XAS, Kleiner et al.[151] obtained similar results on NCA (Ni 3d orbitals hybridized with O 2p orbitals).

2.5. First Cycle Activation of HE-NCM

Depending on the underlying micro/nanostructural picture, the interpretation, particularly of results from electrochemical investigations, might be biased. For example, in the case of the two-phase nanocomposite $0.5Li_2MnO_3 \cdot 0.5LiNi_{1/3}Co_{1/3}Mn_{1/3}O_2$, the Li_2MnO_3 part is initially electrochemically inactive, since

**ADVANCED
SCIENCE NEWS**

www.advancedsciencenews.com

**ADVANCED
MATERIALS**

www.advmat.de

Mn^{4+} is already in its highest oxidation state and cannot be oxidized further. Consequently, in many literature reports, a "classical" activation of Li_2MnO_3 during the initial high-voltage charging above 4.5 V of kind[117]

$$Li_2MnO_3 (\text{EC-inactive}) \rightarrow MnO_2 (\text{EC-active}) + \text{“}Li_2O\text{”} (\text{irreversible loss})$$

(1)
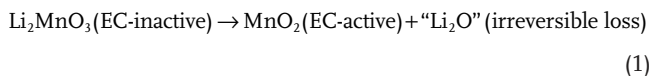
is proposed together with the assumption that oxygen is irreversibly released from the lattice during the activation process.[64–66,81,152–155] The activation is believed to be connected with the initial voltage plateau at about 4.5 V during charging. However, even if all of the Li_2MnO_3 is activated, the measured capacity (activated MnO_2 plus NCM) would not be sufficient to account for the "anomalously" large reversible discharge capacities achieved using this material class. Instead, contributions from reversible oxygen redox processes to charge compensation need to be considered and are widely discussed for Li-rich layered oxide CAMs among many other open questions, especially associated with the initial formation cycle, but also concerning degradation mechanisms.[67–69,118,156]

During the initial charge cycle of the pristine material (up to about 4.8 V), there is, at first, an s-shape-like voltage profile that is attributed to the oxidation of Ni and Co from +II and +III, respectively, to +IV.[108,157,158] The following voltage plateau around 4.5 V and the final small capacity charging period up to the upper COV is related to irreversible structural rearrangements, including loss of long-range "honeycomb" ordering (note that the superstructure reflections disappear after the voltage plateau), loss of chemically available lithium sites (irreversible capacity loss comparing first charging and discharging), and at least partial loss of lattice oxygen. A large variety of structural and/or electronic changes are associated with the irreversible changes during the initial activation process, e.g., reversible oxidation of oxygen species[159] and probably condensation to peroxide-like units,[159] transition metal migration into tetrahedral sites[81,160] and formation of a spinel-like surface layer,[161] formation of lithium/transition metal dumbbells,[70,162] Li^+/H^+ exchange,[163] formation of dislocations[164] etc. All these observations are supposed to play a role in the charge compensation mechanism, the electrochemical hysteresis, and finally also in the degradation (in the form of an average voltage decay and capacity fading). So far, a coherent picture that is capable to explain all these points is still lacking.

Profound investigations into the nanostructure of "layered–layered" NCM composite CAMs and their correlation with electrochemical characteristics regarding the initial formation cycle as well as the long-term degradation have been performed during the past years by Riekehr et al.[71,165] Li-rich NCM materials with nominal composition $cLi_2MnO_3 \cdot [1 - c]LiNi_{1/3}Co_{1/3}Mn_{1/3}O_2$ (with $c = 0.3$, 0.5, and 0.7) were prepared by co-precipitation and molten salt routes. For $c = 0.5$, also the synthesis parameters were varied with the intention to prepare different types of nanostructures for the same overall composition. Most valuable information about the nanostructure of these materials was obtained by (HR)TEM, allowing to detect coherently embedded Li_2MnO_3-like nanodomains with altered cation ordering compared to the NCM host matrix and stacking faults within these domains. Sophisticated evaluation of the $C2/m$-related superstructure

reflections, stemming from these Li_2MnO_3-like domains, was done using the DIFFaX[114] program, which allows to simulate diffraction patterns of crystal structures with 2D defects in particular.

To demonstrate how the nanostructure of pristine Li-rich layered oxide CAMs affects the first cycle electrochemical characteristics, namely the first charge capacity, irreversible initial capacity loss, and reversible discharge capacity, three samples with identical average composition $c = 0.5$, produced either by molten salt route ("MS55") or by co-precipitation ("CP55-1" and "CP55-2"), are compared to one another. Note that the diffraction patterns of these materials are quasi identical, except for subtle differences in the comparably very weak $C2/m$-related superstructure reflections. The dot-like contrast, representing Li_2MnO_3-like domains in the HRTEM image of the "MS55" particle, is virtually restricted to single Li/TM layers that are embedded within the NCM host matrix with line contrast (**Figure 4**a). This is consistent with the extreme and anisotropic broadening of the $C2/m$ superstructure reflections in the corresponding XRD and SAED patterns (**Figures** 4a and 5a). From DIFFaX fitting, the in-plane Li_2MnO_3 domain size and the defect-free stacking range are determined to be about 100 Å and 3–5 TM layers, respectively. The SAED pattern of the "CP55-1" particle shows streaked scattering intensity of the $C2/m$ symmetry, superimposed by discrete $C2/m$ reflections, which can be indexed according to the $[-1-10]_m$, $[-110]_m$, and $[100]_m$ zone axes (Figure 4b, blue arrows). In the bright-field image, defect-free areas can be observed in addition to other areas with stacking fault contrast. The dark-field image assigns the defect-free regions to $C2/m$ symmetry, while in the residual areas, the platelet-shaped Li_2MnO_3-like domains are evenly dispersed, forming a nanocomposite. By evaluating the images of several particles, the size of defect-free blocks was measured as between 100 and 800 Å in the c_h direction and the diameter was mostly defined by the particle dimensions in the $a_h b_h$-plane. The defect-free blocks occupy around 25–30% of the particle volume. The energy-dispersive X-ray (EDX) spectrum obtained on these blocks reveals lower intensity of the Ni Kα and Co Kα peaks compared to the nanocomposite area (Figure 4b). This indicates that the composition in the monoclinic blocks has shifted toward Li_2MnO_3-like, but with significant amounts of Co and Ni incorporated. From the dark-field contrast, the dimensions of the Li_2MnO_3-like platelets in the nanocomposite areas seem to be larger in diameter and follow the stacking direction for "CP55-1" than "MS55." DIFFaX analysis of the $C2/m$-related reflections provides domain sizes of about 330 Å and domain thicknesses of 3–11 TM layers (range 1) and 100 TM layers (range 2) for "CP55-1" (Figure 5b). The different nanostructures of "MS55" and "CP55-1" with equal average chemical composition affect the electrochemical first cycle characteristics. While both samples show nearly the same specific charge capacity up to 4.8 V of 305 mAh g^{-1} ("MS55") and 316 mAh g^{-1} ("CP55-1"), the irreversible capacity loss is only 32 mAh g^{-1} for "MS55," compared to 92 mAh g^{-1} for "CP55-1," leading to a considerably larger (reversible) specific discharge capacity of 273 mAh g^{-1} ("MS55"), compared to only 224 mAh g^{-1} for "CP55-1." The quantified nanostructural parameters (Li_2MnO_3-like in-plane domain size and defect-free layer stacking) of another compositionally identical sample
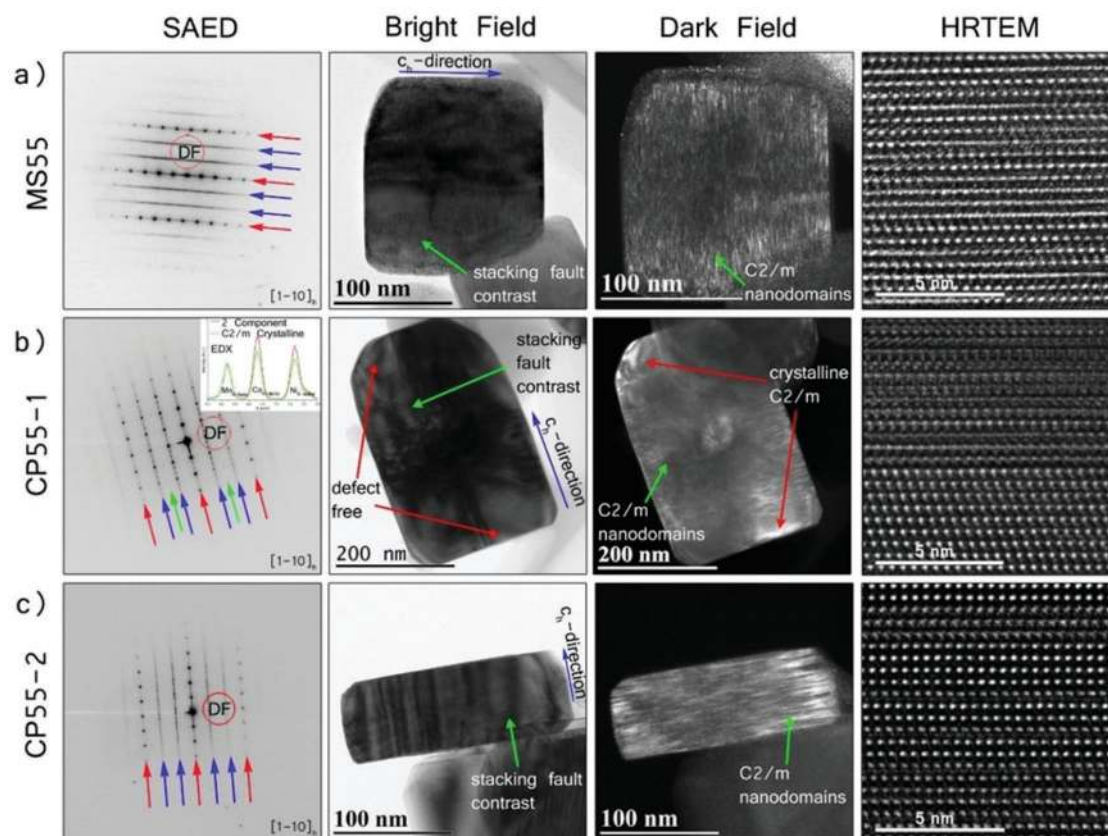
**ADVANCED
SCIENCE NEWS**

www.advancedsciencenews.com

**ADVANCED
MATERIALS**

www.advmat.de

Figure 4. TEM analysis of three different HE-NCM samples: a) "MS55," b) "CP55-1," and c) "CP55-2" with same average composition $0.5Li_2MnO_3 \cdot 0.5LiNi_{1/3}Co_{1/3}Mn_{1/3}O_2$. All particles are oriented to the $[1-10]_h$ zone axis. The red arrows in the SAED patterns denote the positions where intensities of the $R\bar{3}m$ and $C2/m$ symmetries coincide. The reflections highlighted by blue arrows stem exclusively from the $C2/m$ symmetry. The bright- and dark-field images reveal the stacking fault contrast and Li_2MnO_3 nanodomain arrangement in the composite structure, respectively. The HRTEM images show the defect-free stacking sequences of the $C2/m$-like nanoplatelet domains. a–c) Reproduced with permission.[165] Copyright 2016, Elsevier.

("CP55-2") lie between those determined for "MS55" and "CP55-1." As a consequence, also the first cycle specific charge capacity and irreversible capacity loss exhibit intermediate values, thus supporting the hypothesis that the nanostructure significantly affects the electrochemical properties. Given the assumption that the capacity loss is related to the activation of Li_2MnO_3 in the form of a densification process that is again connected with an irreversible oxygen loss at the surface, the following effect of nanostructure on the electrochemical properties can be deduced: In contrast to sample "CP55-1" with coarse Li_2MnO_3-like domain distribution and strong contribution by classical activation (densification), as described by Equation (1), sample "MS55" with very fine dispersed Li_2MnO_3-like domains (high degree of stacking faults) predominantly contributes by reversible oxygen redox activity (oxygen electronic band and/ or peroxide species) to the charge compensation mechanism. The "electrochemically (EC)-active Li_2MnO_3 contribution" as a measure of reversible oxygen redox activity[165] is determined to 115 mAh g^{-1} for "MS55," compared to only 6 mAh g^{-1} for "CP55-1." Correlating the results of the nanostructure analysis with the electrochemical features of the three stoichiometrically similar materials leads to the conclusion that a fine and regular distribution of small platelet-shaped domains with a high degree of stacking faults in the nanocomposite arrangement

is beneficial for achieving large (reversible) specific discharge capacities. Even though the exact electrochemical processes during the activation plateau of Li-rich NCM CAMs are not probed directly, these results indicate a reversible participation of oxygen in the redox processes next to formation of $LiMnO_2$, thus explaining the anomalous capacity provided by an "EC-active" Li_2MnO_3 phase. This work demonstrates the importance of composition and nanodomain arrangement in Li-rich composite structures to enable first cycle specific discharge capacities >250 mAh g^{-1}.

2.6. Crystallographic and Electronic Fatigue of Ni-Rich Layered Oxides

During the course of cycling, the structural change (and therefore the mechanical strain) in CAMs leads to fatigue of the host structure and eventually to capacity fading. The material fatigue of NCA was studied in considerable detail by Kleiner et al.[166] via synchrotron-based in situ XRD using a special cell setup.[167] Pristine samples as well as fatigued samples, cycled for 34 weeks at 50 °C between 40% and 80% SOC, were considered for the experiment. During the in situ measurement, the NCA was cycled at a rate of C/3 in the voltage range from 2.8 to
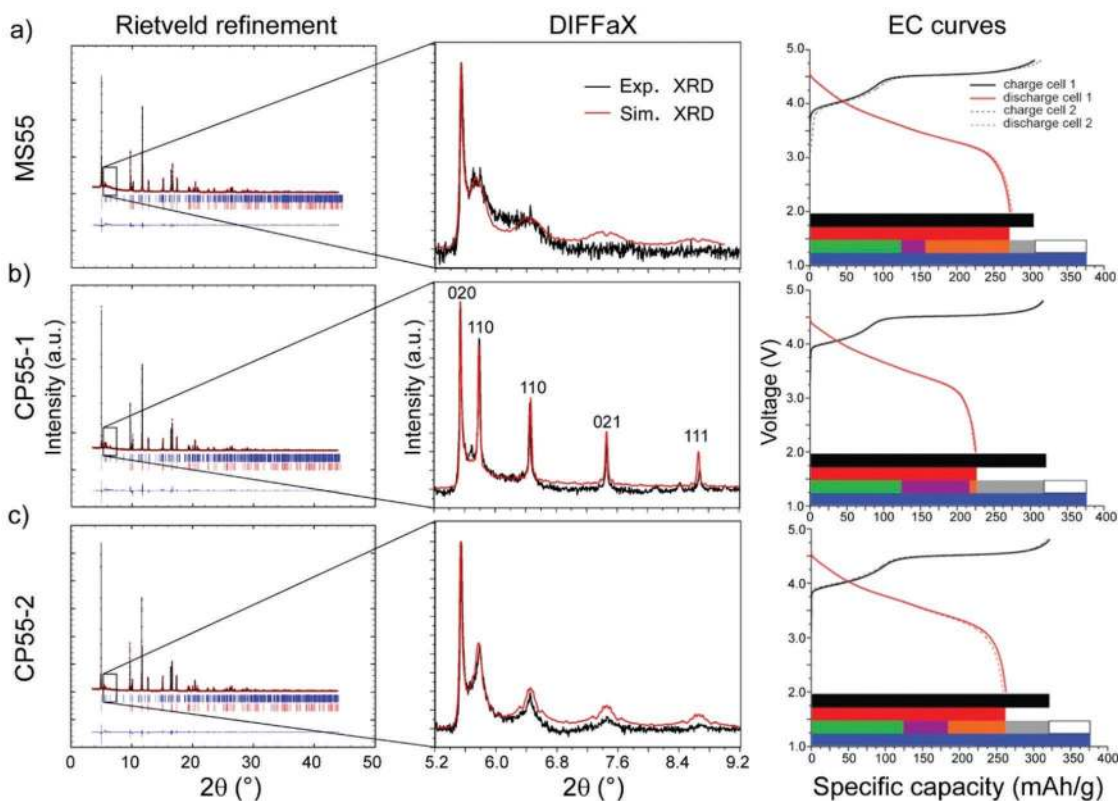
Figure 5. Synchrotron-based XRD patterns of three different HE-NCM samples: a) "MS55," b) "CP55-1," and c) "CP55-2" with same average composition $0.5Li_2MnO_3 \cdot 0.5LiNi_{1/3}Co_{1/3}Mn_{1/3}O_2$. Left: Rietveld refinements together with the corresponding difference curves; vertical tics denote the position of the allowed reflections ($R\bar{3}m$ and $C2/m$). Middle: DIFFaX simulations to $C2/m$-related reflections. Right: First cycle charge/discharge curves. Theoretical specific charge capacity in blue, experimental specific charge capacity in black, experimental specific discharge capacity in red, irreversible capacity loss in gray, EC-active NCM in green, EC-active $LiMnO_2$ in purple, EC-active Li_2MnO_3 in orange, and EC-inactive Li_2MnO_3 in white. a–c) Reproduced with permission.[165] Copyright 2016, Elsevier.

4.1 V vs Li$^+$/Li and XRD patterns were taken every 90 s with an acquisition time of 5 s. **Figure 6**a,b shows the pattern evolution for the pristine and fatigued CAM. In both samples, the extraction and intercalation of Li results in a shift of the reflections, typical of layered oxides.

In the case of the pristine sample, the main phase was assigned as rhombohedral rh1 phase. Surprisingly, a splitting in all reflections can be seen at potentials above 3.6 V, indicating the presence of an additional rhombohedral phase rh2. According to the lattice parameters, the rh2 phase is less delithiated during charging or, in other words, still contains more intercalated Li than rh1. At the end of charge and discharge, only rh1 was detected, which implies that the presence of the rh2 phase does not affect the capacity of the pristine material. In the case of fatigued NCA, the intensity of the rh2 reflections is more pronounced, thereby demonstrating the increasing fraction of differently delithiated particles in the electrode. Besides, an additional phase is observed at potentials below 3.6 V, which was assigned as rh3 phase and is assumed to have a higher degree of delithiation than rh1. During cycling, the rh2 and rh3 reflections remained at nearly identical positions, indicating that the additional rhombohedral phases are neither oxidized nor reduced. Figure 6c,d shows the lattice parameters of all phases present in the pristine and fatigued NCA upon cycling. Only the rh1 phase reveals changes in lattice

parameters, whereas those of the additional phases remain more or less the same. In contrast to the pristine CAM, the rh2 phase is present until the end of charge in the fatigued NCA case. Here, the rh2 content was determined to be 27%, which is in good agreement with the measured capacity loss of 26%. The presence of additional rhombohedral phases was also verified by XAS.[166] Changes in the Ni spectra indicate differently degraded CAM and that part of the material, presumably rh2, does not participate in the electrochemical reactions.

Figure 7 presents a schematic illustration of the oxidation/reduction processes occurring in the NCA particles. As it is more difficult to extract Li from the inner parts of secondary particles, it is assumed that the Li-richer rh2 domains are rather located in the core. The rh3 domains are then expected to be present in the outer parts of the secondary particles, as they are more delithiated. The study clearly demonstrates the heterogeneous charge transfer properties of an electrode, leading to local differences in the degree of (de-)lithiation. Results from Gent et al.[168] corroborate these observations even for low-Ni NCM. They demonstrated that domains within the same NCM111 secondary particle can vary in their Li content by over 10% and assume that this variation is likely even greater in three dimensions. Ultimately, the heterogeneous (de-)lithiation does also affect the individual volume change of cathode particles, and therefore the degree of mechanical strain they are
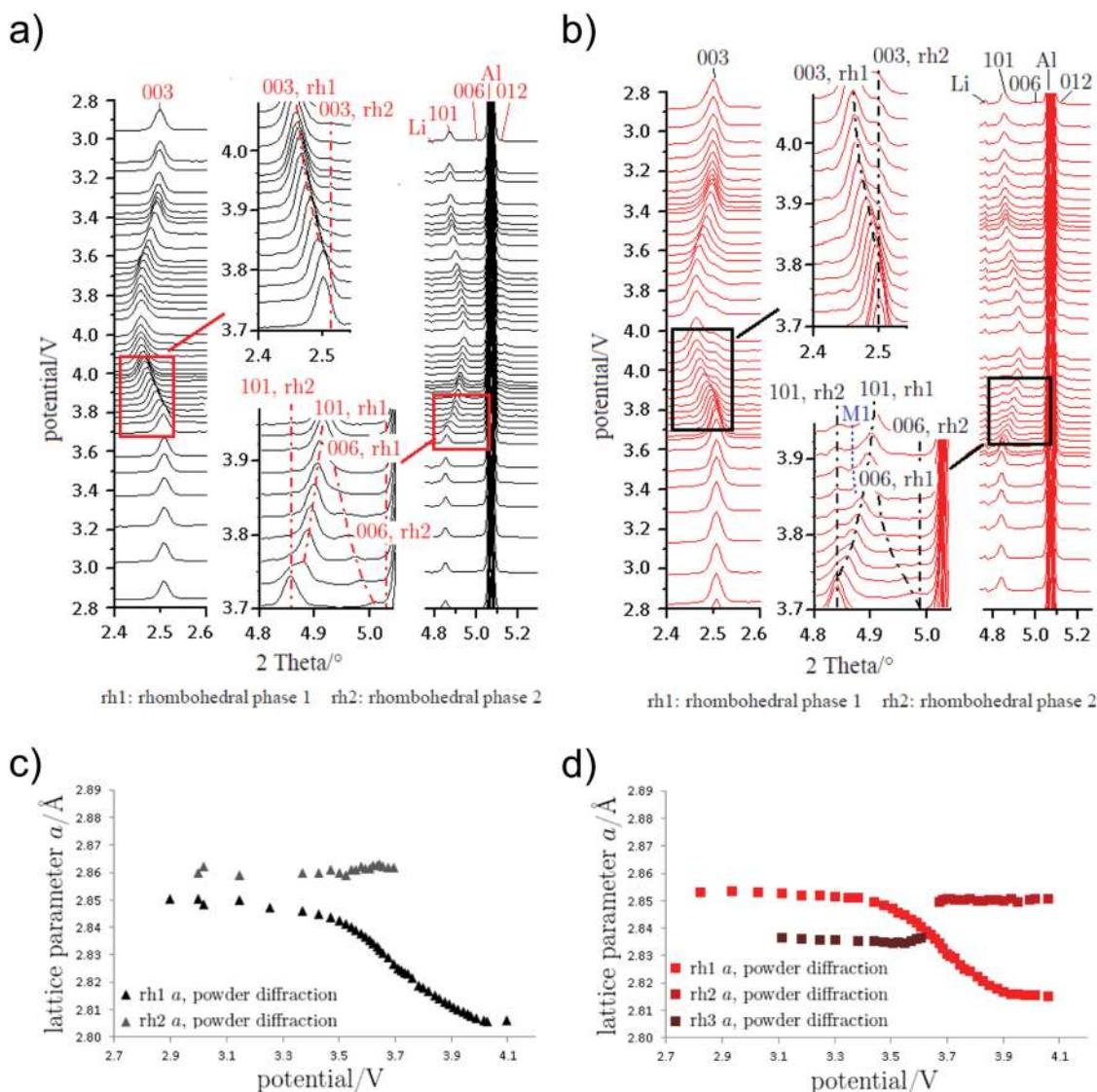
Figure 6. a–d) Synchrotron-based in situ XRD on NCA showing the evolution of diffraction patterns during cycling of pristine (a) and fatigued (b) CAM as well as lattice parameter changes of different NCA phases in pristine (c) and fatigued (d) CAM with charging. a–d) Adapted with permission.[166] Copyright 2015, Elsevier.

exposed to. Local differences in volume change also increase the strain at the boundaries between differently delithiated domains, which further accelerates the mechanical degradation. Kleiner et al.[166] assumed that the presence of differently delithiated phases arises from side products, for example rock-salt-like phases on the particle surface, that impede the Li-ion transport (note that overpotentials affect the effective upper and lower COVs), thereby adversely affecting the accessible capacity during galvanostatic cycling. Similar results have been reported by Liu et al.[169] High-Ni NCM and NCA CAMs suffer from severe capacity loss, particularly due to irreversible phase transformations on the particle surface.[170] Galvanostatic intermittent titration technique (GITT) measurements by Kleiner et al.[151] revealed an increase in overpotential of fatigued NCA electrodes, which is attributed to changes in the surface morphology, most likely due to formation of NiO-like layers. The

formation of rock-salt-type NiO was also clearly demonstrated and directly observed on the atomic scale in HE-NCM using scanning TEM imaging by Boulineau et al.[171] and reported in many other studies for NCM and NCA.[91,144,146,172–175] Advanced in situ TEM measurements were performed by Hwang et al., showing the decomposition of NCA at different SOCs. The results provide evidence that significant changes occur in charged NCA, arising from highly reactive Ni^{4+} species at high SOC. Also, transformation from the layered to spinel phase is likely since layered $LiTMO_2$[109–111] and spinel $LiTM_2O_4$ materials share the same ccp oxygen framework (rhombohedrally distorted for $LiTMO_2$) with an interlayer distance of about 4.7 Å. A comprehensive demonstration of the cation exchange process was given by Bak et al.[53] The disordered layer is believed to increase the resistance and impair the electrode performance.[31] Remarkably, Lin et al.[176] reported
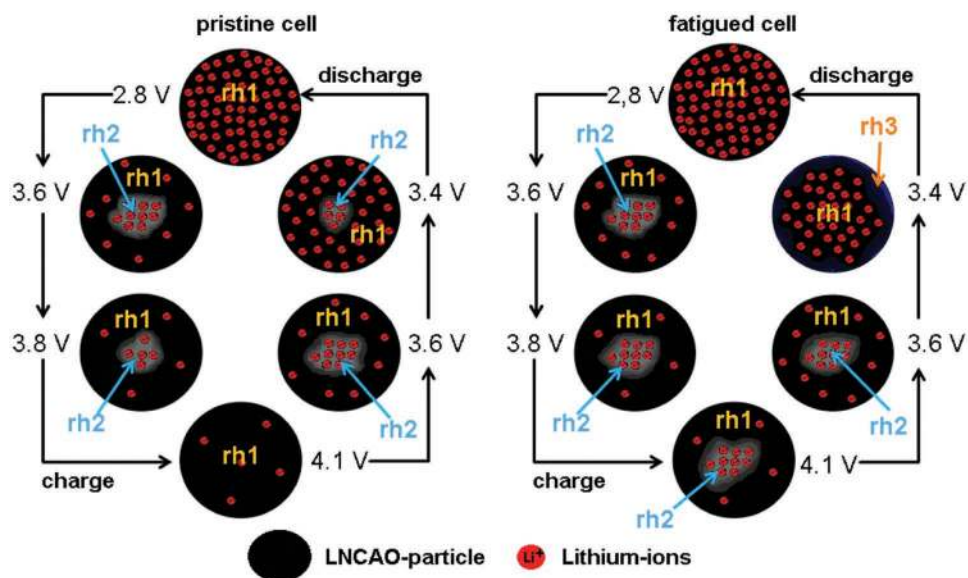
ADVANCED
SCIENCE NEWS
www.advancedsciencenews.com

ADVANCED
MATERIALS
www.advmat.de

Figure 7. Schematic illustration of oxidation/reduction processes in pristine and fatigued NCA with differently active phase fractions rh1, rh2, and rh3. Reproduced with permission.[166] Copyright 2015, Elsevier.

a structural reconstruction (layered to rock-salt to spinel) and chemical evolution of a surface layer on Ti-doped NCM ($LiNi_{0.4}Co_{0.18}Mn_{0.4}Ti_{0.02}O_2$) particles solely due to electrode–electrolyte interaction without the necessity of electrochemical activation. An impedance rise was already observed after exposure of the NCM electrode to the electrolyte. Nevertheless, they also showed that surface reconstruction is more severe at more dynamic cycling. Furthermore, the study revealed that the surface reconstruction strongly depends on the upper COV as well as the crystal orientation. Thicker layers were found particularly along lithium diffusion channels relative to other orientations, thus suggesting that surface reconstruction is promoted by lithium removal during charging. In contrast to the widely reported core–shell structures,[91,172,177,178] Zhang et al.[179] showed that the formation of rock-salt and spinel-like phases also occurs in the bulk of Ni-rich layered transition metal oxides, leading to formation of an "anti-core–shell" structure. The oxygen loss caused in the reducing environment at the cathodic SEI indirectly results in removal of oxygen in the inner particle regions via outward diffusion from the bulk to the oxygen-depleted surface region. Thereby, defects are formed in the bulk, while the surface still remains as the layered phase. Nevertheless, the TEM study that analyzed around 120 particles revealed that the majority (90%) of the particles have a core–shell structure and only 10% were found to develop the "anti-core–shell" structure.

3. Long-Term Fatigue and Degradation

3.1. Mechanical Degradation of Ni-Rich NCM

Because of the changes in crystal structure in Ni-rich NCMs, the mechanical degradation processes, such as formation of microcracks and cathode self-pulverization, are a major cause of capacity fading, especially at high charging rates.[145,169] The large volume changes occurring during lithiation and delithiation (Figure 3a) are believed to be responsible for the buildup of considerable mechanical stress inside the CAM particles. The volume changes of NCM811 upon charging and discharging on the secondary particle level were visualized by Kondrakov et al.[28] by use of in situ light microscopy. **Figure 8**a shows a part of the top surface of an electrode with several secondary particles. For comparison, a representative SEM image is shown in Figure 8b. The relative changes in secondary particle size as a function of half-cell potential and Li content in the electrode were determined by digital image correlation. A significant irreversible volume change was detected in the first cycle. Because operando XRD did not reveal any anomalies in the first cycle, it is concluded that effects, such as cathodic SEI formation, contribute initially to the volume increase. Figure 8c depicts the (reversible) volume changes observed in the second cycle. A direct correlation was found between the changes in secondary particle size and those deduced from the unit cell volume by XRD (Figure 3). The most pronounced volume changes were seen at potentials above 4.0 V vs Li^+/Li, where a sudden shrinkage of the secondary particles occurs, in agreement with the unit cell volume behavior. Figure 3a also shows the crystallographic strain (anisotropic microstrain parameter S_{202}) derived from operando XRD data based on Bragg reflection broadening and fitting using an anisotropic strain model.[28] The calculated values indicate that the NCM811 is subjected to more severe buildup of microstrain during cycling. The S_{202} profiles confirm that the lattice changes occur in a heterogeneous manner at high degrees of delithiation, presumably due to variations in lattice parameters among individual domains. Due to the anisotropic volume changes and the different orientations of crystallites (primary particles), the secondary particles experience different net strain. Intergranular cracks are frequently observed in cycled electrodes.[28,90,145,169,173,180,181] By discrete element method on a cohesive crack model, Sun et al.[90] showed that bipolar (i.e., anisotropic) expansion/contraction
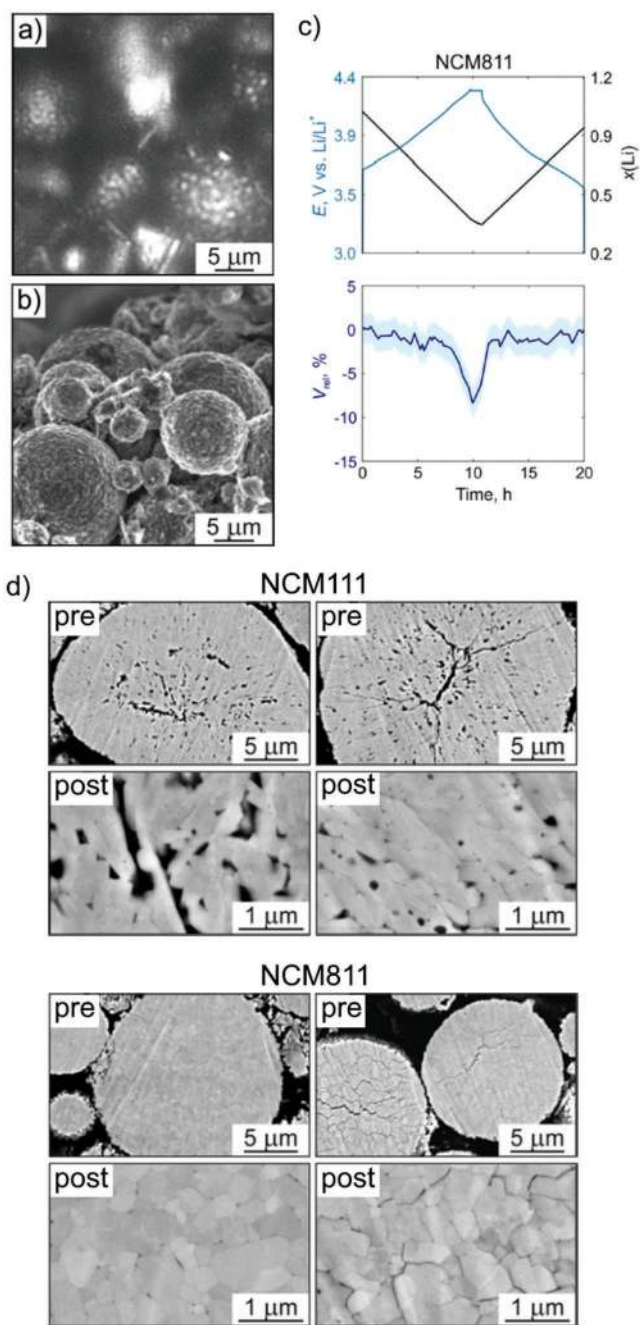
Figure 8. a) Representative in situ light microscopy image and b) SEM image of NCM811 secondary particles with micrometer-scale dimensions. c) Changes in secondary particle volume of NCM811 during cycling determined by in situ light microscopy together with the corresponding voltage profile and the evolution of lithium content with time. Shaded areas represent the error margin. d) Cross-sectional SEM images at different magnifications of NCM111 and NCM811 collected before (pre) and after (post) 50 cycles at C/2. a–d) Adapted with permission.[28] Copyright 2017, American Chemical Society.

of primary particles leads to greater damage as a result of tensile stress generation along the grain boundaries. Using in situ electron microscopy, Miller et al.[180] demonstrated how separation at grain boundaries after cycling leads to loss of

connectivity and electrical contact between individual grains in NCA. Figure 8d shows cross-sectional SEM images of both NCM111 and NCM811 collected before and after cycling. In the case of NCM111, the effect of cycling was hardly visible, since already the pristine material revealed a porous microstructure. However, the microcracks observed in NCM811 can be clearly attributed to electrochemical cycling, because such "defects" were not present in the pristine material. Sun and Manthiram[145] also demonstrated the greater susceptibility of particularly Ni-rich NCM CAMs to crack formation. In agreement, several other studies[130,144,147,182] came to similar results, thus demonstrating the higher risk of mechanical failure when using Ni-rich layered oxides as CAM in Li-ion cells. Impedance measurements by Sun and Manthiram[145] revealed that the charge transfer resistance of NCM622 remains basically the same during cycling, whereas that of NCM950505 steadily increases with increasing cycle number. Using advanced TEM, they showed that the formation of a NiO-like layer on the CAM particle surface is predominantly causing the impedance rise. Comprehensive results were obtained by Kleiner et al.[151] for NCA using near-edge X-ray absorption fine structure (NEXAFS) spectroscopy. They showed that more porous, open secondary (particle) structures can reduce the capacity fading.[168,183–185] Such structures are believed to better accommodate volume changes, thus eventually reducing stress during cycling (particularly in the case of SOC heterogeneity).

While intergranular cracks are commonly observed in Ni-rich NCM cathodes,[28,90,145,169,173,180,181] they have been detected only in electrodes cycled to high potentials.[186,187] For example, in the case of NCM622, Yan et al.[186] observed the presence of intragranular cracks in samples cycled to ≥4.65 V vs Li$^+$/Li. Ultimately, they will evolve into larger cracks. Hence, their formation as well as the underlying mechanism(s) must be understood in detail to achieve stable performance and longevity of Ni-rich NCM-based LIBs. TEM studies[186,187] revealed that intragranular cracking follows a strict crystallographic preference along the (003) plane. It was emphasized that edge-dislocations may play an important role, as they constitute nucleation sites and that cracking may therefore be initiated from the grain interior. This observation is in sharp contrast with the general opinion that intragranular cracking is preferentially initiated on grain boundaries or particle surfaces. Furthermore, it was shown by HRTEM that the layered structure transforms into a rock-salt-like phase at the crack surfaces.[186] The presence of Li-site TM cations (rock-salt formation) and a high degree of stacking faults, presumably due to distortion of the oxygen framework (with high vacancy concentration), was also observed by Zhang et al.[188] In any case, a (negative) cooperative effect of oxygen vacancies, structural dislocations, cracking, and rock-salt formation is likely to occur.

Evidently, the choice of voltage range or, more precisely, the upper COV plays a crucial role in the overall degradation behavior, as it controls the degree of delithiation, and therefore the magnitude of volume changes. In most of the literature reports, CAMs are benchmarked for a given voltage range or specific SOC.[17,18] Jung et al.[91] demonstrated the significant impact of COV on the degradation of NCM523. It was shown that the material suffers from more or less irreversible transformations and increasing surface resistance depending on the

**ADVANCED
SCIENCE NEWS**

www.advancedsciencenews.com

**ADVANCED
MATERIALS**

www.advmat.de

COV, presumably due to structural instability at high potentials. However, it was also emphasized that the type of COV-dependent structural degradation strongly varies with the actual CAM composition. A systematic analysis on the role of COV and composition was provided by Sun and Manthiram[145] for NCM622 and NCM950505. Another, more application-relevant way to benchmark different CAMs is the comparison with regard to energy density (particularly important for the electric vehicle sector). NCM111 and NCM811, for example, are capable of providing similar energy densities when charged to specific COVs. A comprehensive overview of the volume changes of high- and low-Ni NCM CAMs for different degrees of delithiation (or energy densities) was given by de Biasi et al.[61] **Figure 9**a shows the upper COV for different NCMs that is required to achieve a comparably high specific energy density of 750 Wh kg^{-1} ($U_{max(750\,Wh\,kg^{-1})}$), calculated from the specific capacity and the average voltage. The solid data points in Figure 9b display the corresponding relative change in unit cell volume upon charging to $U_{max(750\,Wh\,kg^{-1})}$. It is apparent that CAMs with a higher Ni content still exhibit larger shrinkage. However, in contrast to when the materials are charged to the same upper COV of 4.3 V (hollow data points), the relative volume change increases in a linear fashion with increasing Ni content. Notably, when the samples are cycled in the range between 3.0 V and $U_{max(750\,Wh\,kg^{-1})}$ tailored for comparable energy density, Ni-rich NCMs reveal much better capacity retention than low-Ni content CAMs (Figure 9c). This result establishes that the overall cycling performance is not only dependent on the structural stability of the electrode material used, but is also affected by other factors.

3.2. Degradation Mechanism of HE-NCM

Very fine and evenly dispersed platelet-shaped Li$_2$MnO$_3$-like nanodomains with high degree of stacking faults, as observed for pristine "MS55," lead to a higher anionic redox activity via the oxygen electronic band (localized formation of peroxide species has not been proven for 3d TM-based materials yet) and cause smaller irreversible oxygen loss. For "CP55-2" with larger Li$_2$MnO$_3$-like domains, irreversible oxygen loss is higher during the initial formation and anionic redox activity is reduced. Both processes, irreversible oxygen loss and reversible oxygen contribution, are supposed to be present in the active materials at the same time, but with different fractions, determined by the pristine nanocomposite arrangement.

Overall, our work contributed to a better understanding of the degradation mechanisms of Li-rich layered CAMs by revealing the existence of a nanotwin domain structure, even directly after the first electrochemical cycle, which is supposed to represent a kind of intermediate state toward the spinel phase formation with long-term cycling. Because a nonisomorphic cubic supergroup of $R\bar{3}m$, for example the $Fm\bar{3}m$ rock-salt structure, offers four degrees of freedom (four space diagonals of the cubic cell) to represent a rhombohedral c_h-axis (index h for hexagonal lattice), twin domain formation is expected, especially since the rhombohedral distortion of Li-rich NCM CAMs is only very small (typical c/a ratio is 4.95–5.00 and pseudo cubic setting would correspond to $c/a \approx 4.89$). Twins are defined
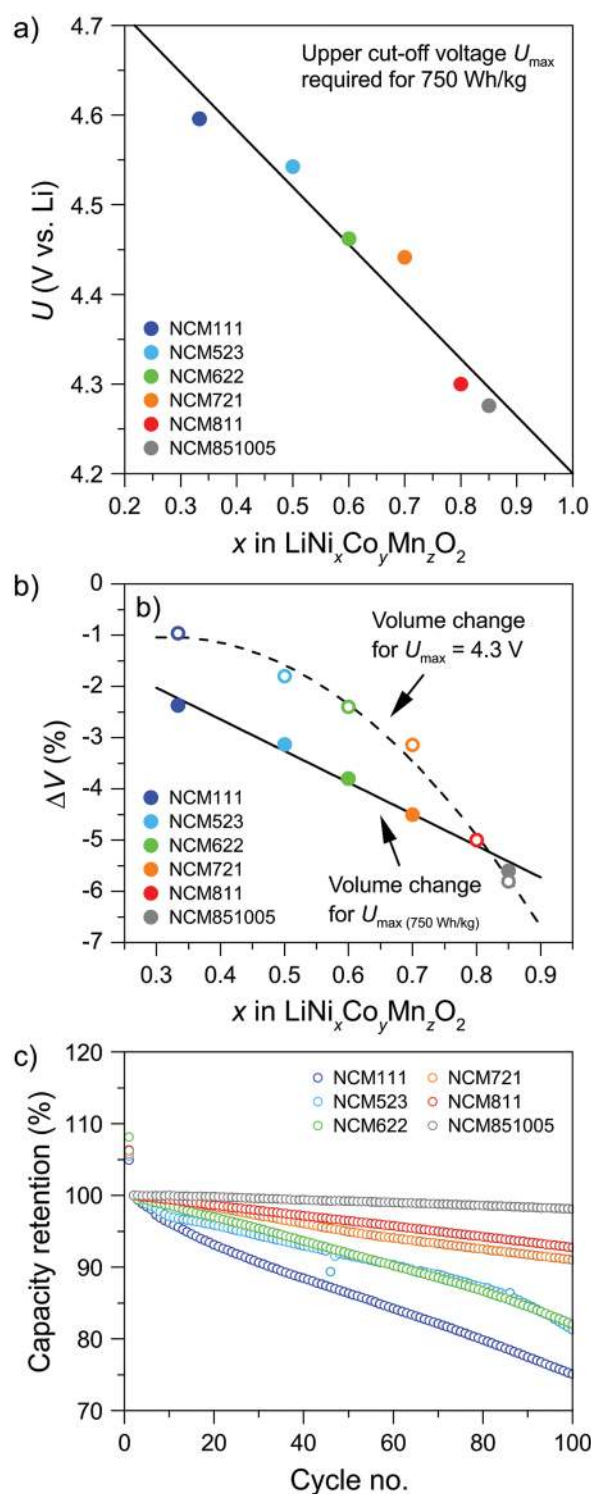

Figure 9. Relationship among upper cutoff voltage, gravimetric energy density, crystallographic volume change, and capacity retention for different NCM CAMs. a) Upper cutoff voltage (U_{max}) as a function of Ni content required to achieve the gravimetric energy density of NCM811 at 4.3 V ($\approx$750 Wh kg^{-1}). b) Relative changes in unit cell volume at 4.3 V and for $U_{max(750\,Wh\,kg^{-1})}$. c) Capacity retention based on the second cycle discharge capacity when cycled in the range between 3.0 V and $U_{max(750\,Wh\,kg^{-1})}$. a–c) Adapted with permission.[61] Copyright 2017, American Chemical Society.

ADVANCED
SCIENCE NEWS
www.advancedsciencenews.com
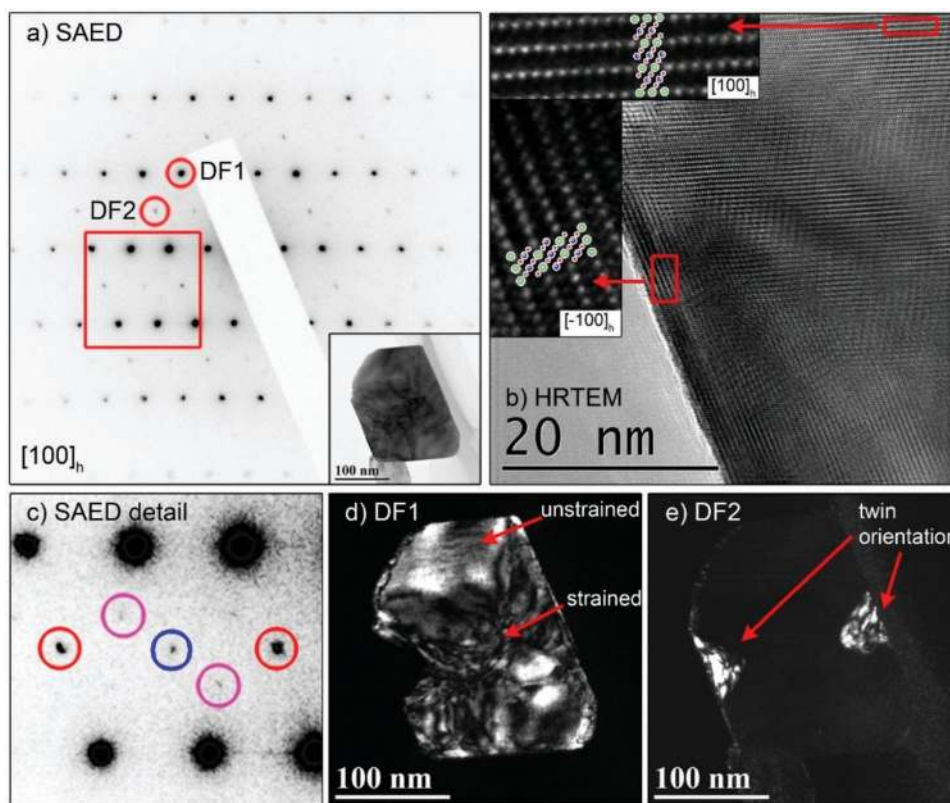
ADVANCED
MATERIALS
www.advmat.de

Figure 10. TEM twin analysis of a pristine "MS55" particle in $[100]_h$ orientation. a) SAED pattern with strong reflections of the $[100]_h$ main orientation and weak reflections of the $[-100]_h$ twin orientation. b) HRTEM pattern of the twin boundary. c) Detail of the SAED pattern and increased contrast with reflections of the $[100]_h$ main orientation, the $[-100]_h$ twin orientation (red), the $[101]_m$ monoclinic twin orientation (magenta), and the $[121]_c$ spinel-like orientation (blue). d) Dark-field (DF1) image with the $[100]_h$ main orientation excited. e) Dark-field (DF2) image with the $[-100]_h$ twin orientation excited. a–e) Reproduced with permission.[71] Copyright 2016, Elsevier.

here as domains or crystallite parts with alternative rhombohedral c_h-axis orientations that define the direction of Li- and TM-layer stacking in relation to the "main rhombohedral axis" of the layered matrix material.

Taking the existence of rhombohedral twin orientations into account is very important for an adequate structural description of Li-rich NCMs, since the corresponding SAED patterns with overlapping contributions from various $R\bar{3}m$ twin domains can easily be misinterpreted to represent $Fd\bar{3}m$ spinel patterns. This is of significant importance, because, based on SAED analyses, it is stated by several research groups that formation of a spinel-like phase occurs in Li-rich nanocomposites already during the initial cycle,[72,73,189] even though a spinel signature in the electrochemical characterization appears only after extended cycling.[73,74] Ito et al. mentioned a twin-like framework in a Li-rich composite after the formation cycle[189] and also Wang et al.[154] described microtwinning for activated Li_2MnO_3. Sathiya et al.[69] revealed anionic redox activity based on peroxide formation in the structurally related $Li_2Ru_{0.5}Sn_{0.5}O_3$ and observed twin- and not spinel-like reflections in SAED patterns after the initial cycle, presumably linking the anionic redox to twin formation. A large number of crystallites of the "MS55" and "CP55-2" pristine materials show macroscopic twinning in the sense that the crystallites are composed of clearly distinguishable large parts with twin relation to each other. These can

be clearly visualized by dark-field TEM imaging if specific selection of twin domain reflections is possible (**Figure 10**).

Without going into detail about the differences between "MS55" and "CP55-2," SAED patterns of both samples show diffraction spots at the $n/3$ position, which are assigned to the $C2/m$ superstructure reflections after the formation cycle with charging to 4.8 V vs Li^+/Li (exemplarily shown for "CP55-2" in **Figure 11**a; denoted by green arrows). This provides evidence that Li_2MnO_3 structure fragments without significant long-range correlation lengths are still present after the formation cycle. The stacking fault contrast observed for pristine samples is no longer detectable in the bright-field images. The loss of long-range translational symmetry between the $LiMn_6$ honeycomb structure elements explains the extinction of the $C2/m$ superstructure reflections in the synchrotron-based XRD patterns after the formation cycle. The scattering spots at the $n/2$ position can be assigned to either a spinel- or a twin-like domain (Figure 11a; denoted by the blue arrow). Contrary to the rather large twin domains in the pristine material, the excited areas in the dark-field images for both the "MS55" and "CP55-2" particles after formation are composed of nanosize and shapeless domains. However, the evaluation of the characterization results for the second charge cycle does not indicate clear spinel-like redox activity, and therefore a considerable fraction of the excited area is to be ascribed rather to
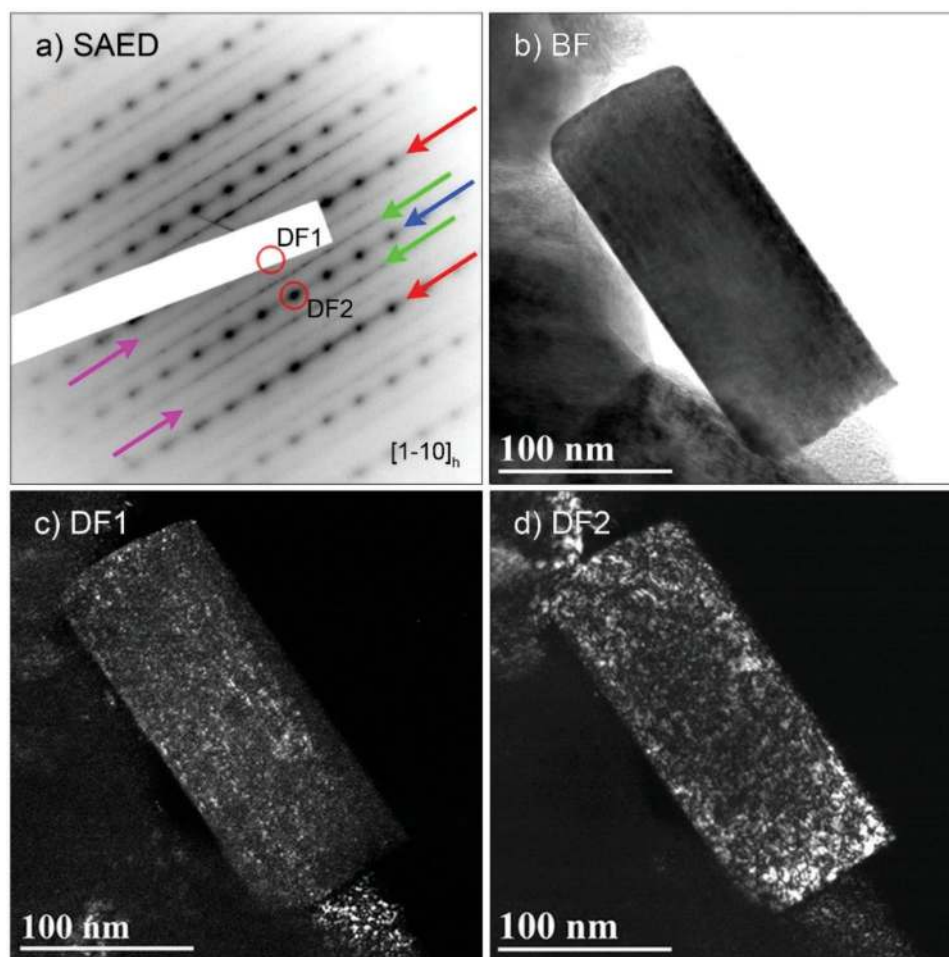
**ADVANCED
SCIENCE NEWS**

www.advancedsciencenews.com

**ADVANCED
MATERIALS**

www.advmat.de

Figure 11. TEM analysis of a "CP55-2" particle after the initial cycle. a) SAED pattern with reflections of the $[1{-}10]_h$ main orientation (red arrows), streaked $C2/m$ superstructure reflections of the quasi-equal monoclinic $[-1{-}10]_m$, $[-110]_m$, and $[100]_m$ orientations (green arrows), spinel/twin-like (blue arrow), and streaked $C2/m$ superstructure reflections of the $[00{-}1]_m$ twin orientation (magenta arrows). b) Bright-field (BF) image of the particle, c) dark-field (DF1) image with the Li_2MnO_3 component in $[00{-}1]_m$ twin orientation excited, and d) dark-field (DF2) image with the spinel/twin-like component excited. a–d) Reproduced with permission.[71] Copyright 2016, Elsevier.

overlapping twin-like orientations than to a spinel phase. The TEM analysis shows drastic changes in the composite structure (twin-like and possibly spinel-like nanodomains) occurring during the formation cycle. The well-defined layered contrast in the HRTEM image verifies that a coherent ccp oxygen lattice, accommodating the various cation arrangements, is maintained in the discharged state. TEM analysis performed after 70 cycles is qualitatively very similar for both samples. The SAED patterns exhibit the $R\overline{3}m$ main reflections and twin/spinel-like reflections at the $n/2$ position. In this case, a clear contribution from a spinel-like phase can be revealed from the cycling data, implying that most of the intensity at the $n/2$ position needs to be considered to be of spinel-like origin.

The structural evolution with further cycling reveals that the formation of an EC-active $LiMnO_2$ component as well as the subsequent spinel formation does not only depend on the irreversible oxygen release in the initial cycle, but is also affected by the reversible anionic redox activity. By entering the 4.5 V plateau, holes are injected into the O 2p band[15,34,75,118,190] and

two mechanisms compete with each other, namely, irreversible oxygen loss and reversible oxygen contribution. The effective formation of EC-active bulk $LiMnO_2$ requires Li_{TM} extraction to open efficient TM migration pathways for material densification.[65] However, before Li_{TM} can be delithiated, Li_{Li} needs to be removed from the Li layer,[191] which is accompanied either by irreversible oxygen loss or by reversible oxygen redox. The nanostructure of pristine "MS55" with very fine dispersed, small Li_2MnO_3 domains of high defect density seems to facilitate reversible oxygen redox as the charge compensation process. Consequently, a high degree of delithiation of Li_{Li} from the Li layer and subsequently of Li_{TM} from the TM layer produces effective migration pathways for TM from the surface to the bulk, thereby allowing densification of the bulk via MnO_2 formation. For "CP55-2" with much coarser nanocomposite structure, the reversible oxygen redox contribution is considerably limited and bulk lithium sites (Li_{Li} and Li_{TM}) cannot be sufficiently delithiated. Here, irreversible oxygen loss is the dominant process and results in dissolution of the oxygen

ADVANCED
SCIENCE NEWS
www.advancedsciencenews.com

ADVANCED
MATERIALS
www.advmat.de

framework at the particle surface,[50,65,192] by which not only Li_{Li} but also surface TM cations are lost.

This work strongly indicates that nanotwinning is the prevalent mechanism of structural transformation during the formation cycle in Li-rich NCM CAMs. The reversible oxygen redox contribution is supposed to be connected with the formation of the observed nanoscale twin-like arrangements, probably by affecting the local strain via creation/annihilation of localized charged anion species (e.g., peroxides for comparable non-$3d$ TM systems, such as $Li_2Ru_{0.5}Sn_{0.5}O_3$). The cation arrangement at a twin boundary is close to that of the spinel structure, and therefore it is likely that continuous creation and annihilation of localized charged anion species cause the nanostructure to transform gradually into a very fine nanotwinned one and finally into the thermodynamically more stable spinel-like phase.[76,193,194] Cell cycling results in unwanted capacity and voltage fade, which is attributed to the appearance of a spinel-like phase. Nanosize twinned structures, acting as a precursor for the spinel-like component, would help explain why the spinel-like component forms faster during cycling in "MS55," where anionic charge compensation is enhanced compared to "CP55-2." To achieve high-energy-density HE-NCM CAMs of good cycling stability, irreversible oxygen release from the surface must be avoided or minimized, e.g., by coating the particles with electrochemically inactive materials, such as Al_2O_3[195–198] or AlF_3[199–201] for example. Furthermore, a high anionic redox contribution realized by a fine dispersed nanostructure should be stabilized in a way that gradual increase of the nanosize twin domain interface (and subsequent transition to a spinel-like phase), causing voltage decay, is suppressed. This can most probably be achieved by an optimized atomic composition through doping with electrochemically active and/or inactive elements, such as Al,[202] Cr,[203] Mg,[204,205] Na,[206,207] Nb,[208] Ru,[209] Y,[210] Zr[211] etc. However, most attempts to reduce the voltage fade to slow or no rate are to make sacrifices on the energy density, especially when doping with electrochemically inactive elements.

Figure 12. a) Pressure measurement system (i) with schematic figures of the custom cell (ii) and the thermostat (iii). b) Voltage profiles and the corresponding pressure evolution of NCM622/graphite cells. The "formation" cycle at C/10 included a 45 °C step. The subsequent cycling was performed at C/2 and at 25 °C (blue) or 60 °C (red). a,b) Adapted with permission.[102] Copyright 2017, American Chemical Society.

4. In Situ Gas Analytics

Many of the degradation mechanisms discussed above are accompanied by gas evolution. In situ pressure analysis is a suitable method to detect gas formation/release based on the changes in internal cell pressure. A custom setup for high-throughput in situ pressure analysis was demonstrated by Schiele et al.[102] and is shown in **Figure 12**a. Within a closed system and at a controlled stable temperature, the pressure changes are monitored via a pressure sensor. To probe the "true" gas evolution with cycling, usually the cell volume is determined first. A representative example of a pressure measurement is given in Figure 12b. Here, the temperature-dependent gas evolution in NCM622 full-cells was studied. During the formation cycle at 45 °C, a pressure increase was detected predominantly due to graphite SEI formation. In the further course of the measurement, the temperature was set to either 25 or 60 °C and the cell was subjected to continuous cycling. At 25 °C, the pressure remained virtually constant. However, during the open-circuit voltage (OCV) period of 5 h at 60 °C (red curve
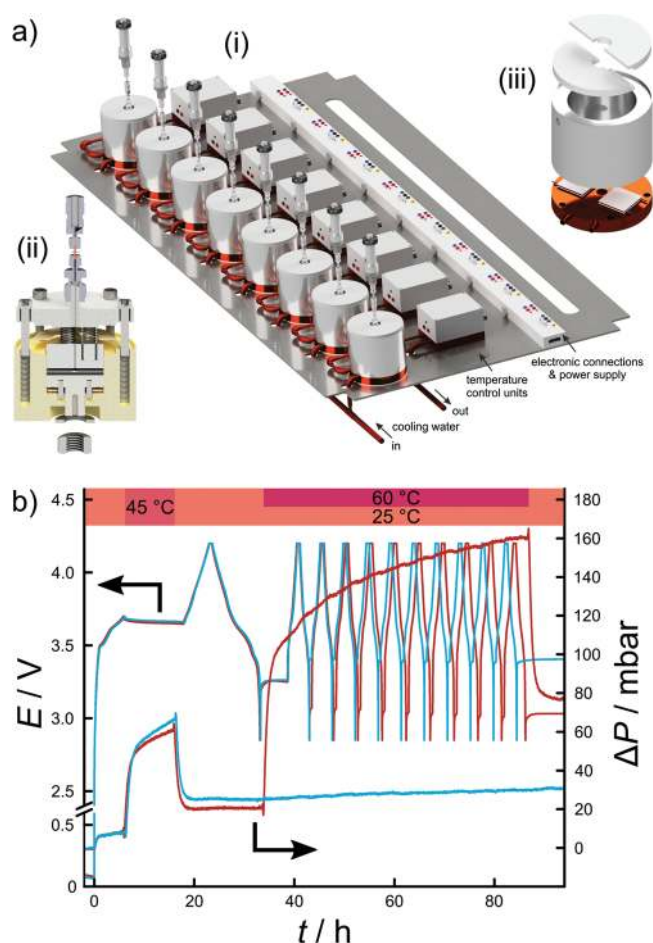
in Figure 12b) the pressure was found to strongly increase at first, and then it continued to increase without reaching a stable value. This pressure increase is believed to be caused by accelerated electrolyte decomposition at elevated temperatures. Closer examination of the pressure curves revealed additional cyclic fluctuations of the internal pressure, which can be attributed to changes in volume of the electrode with Li (de-)intercalation. In fact, in situ pressure measurements have been performed on some anode and cathode materials in the past[102,103,212,213] (on an electrode level) to gain insights into 3D volume changes of practical electrodes. In many of these experiments, $Li_4Ti_5O_{12}$ (LTO), a so-called zero-strain material, was used as the counter-electrode (note that the volumetric changes of LTO during cycling are negligible). By fitting and subtracting the irreversible pressure increase due to gas evolution, the periodic changes in pressure can be correlated to volume changes if the cell volume and the density of the active material are known.

For detailed qualitative and quantitative analysis of the evolved gaseous products, a continuous flow DEMS setup,
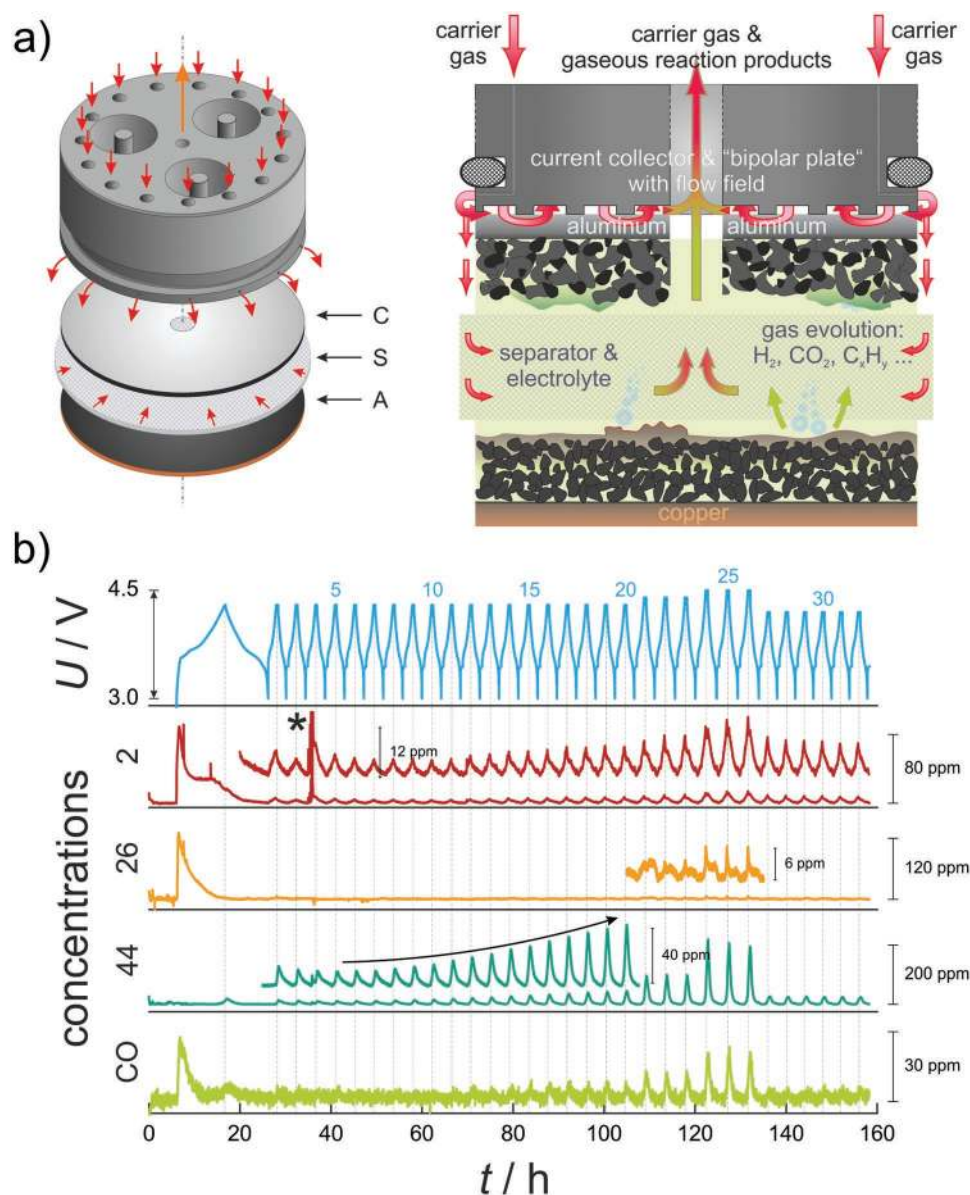
**ADVANCED
SCIENCE NEWS**

www.advancedsciencenews.com

**ADVANCED
MATERIALS**

www.advmat.de

Figure 13. a) Schematic figure of the custom DEMS cell. Reproduced with permission.[55] Copyright 2015, American Chemical Society. b) Long-term test performed on an NCM523/graphite cell using LP57 as the electrolyte. Both the voltage profile and the corresponding MS and IR signals are shown. The asterisk denotes a measurement artifact. Reproduced with permission.[56] Copyright 2016, Springer Nature.

combined with differential electrochemical infrared spectroscopy (DEIRS), was implemented by Berkes et al.[54,55] (**Figure 13**a). The most common gases that evolve in LIB cells during cycling are CO_2, CO, C_2H_4, H_2, and O_2.[56,214,215] A brief overview of their formation mechanisms/origin is given in **Table 1**. In the following, we focus on gas evolution at the cathode side, mainly comprising release of CO_2, CO, and O_2. For the formation of both CO_2 and CO, several mechanisms are proposed and discussed in the literature, including oxidative electrolyte decomposition at the CAM particle surface, Li carbonate decomposition, and chemical reactions of lattice oxygen with electrolyte molecules.[216]

For example, NCM523/graphite cells cycled between 3.0 and 4.3 V were analyzed using the aforementioned DEMS system,

which is clearly suited for testing electrode materials under realistic operating/cycling conditions.[56] Figure 13b shows the measured signals for H_2 ($m/z = 2$), C_2H_4 (26), CO_2 (44), and CO. Of note, by studying the electrodes in half-cells, the origin of the different gases could be identified in an indirect manner. H_2, C_2H_4, CO_2, and CO mainly evolved at the anode at the beginning of charging due to SEI formation. CO_2 and CO also appeared at the upper COV in every cycle, and therefore they are believed to originate from oxidation of electrolyte. An increase in CO_2 and CO signals was observed when the upper COV was increased to 4.4 or 4.5 V (cycles 21–26 in Figure 13b), thus indicating accelerated electrolyte decomposition. Especially Ni^{4+} species, present in NCM CAMs at high SOC, are highly reactive and presumably cause oxidative electrolyte degradation,

ADVANCED
SCIENCE NEWS

www.advancedsciencenews.com

**ADVANCED
MATERIALS**

www.advmat.de

Table 1. Summary of gaseous reaction products in LIBs.

Species	Origin	Refs.
CO_2	- SEI formation (anode)	[56]
	- Oxidative electrolyte decomposition (cathode)	[100,217]
	- Li_2CO_3 (cathode)	[216]
	- Reaction of lattice oxygen with electrolyte (cathode)	[216]
	- Reductive EC:DMC decomposition (anode)	[218]
CO	- SEI formation (anode)	[56]
	- Reaction of lattice oxygen with electrolyte (cathode)	[219]
O_2	- Lattice oxygen (cathode)	[101,219,220]
H_2	- Trace water and protic electrolyte constituent reduction (anode)	[56,221,222]
C_2H_4	- SEI formation (anode)	[56,221,223,224]
POF_3	- $LiPF_6$ (cathode)	[225]

and therefore cathodic SEI formation.[54–56,59,60] In situ gas analysis performed by Hatsukade et al.[216] on NCM with ^{13}C-labeled Li_2CO_3 clearly demonstrated that also Li_2CO_3 decomposition contributes to CO_2 evolution, particularly during the first charge cycle. At the same time, the study revealed a greater contribution from electrolyte decomposition, as indicated by significant [12]CO_2 release. Jung et al.[219] proposed that both the evolved CO_2 and CO are mainly due to chemical reaction of lattice oxygen from the NCM CAM with the electrolyte solvent(s). Likewise, based on combined heating and TEM experiments, Wu et al.[128] showed for NCA that O_2 evolution is indeed due to release of lattice oxygen because of the rapid growth of a rock-salt-type structure on the top surface according to

$$2\ TMO_2\left(layered\right) \rightarrow 2\ TMO\left(rock\text{-}salt\right) + O_2 \qquad (2)$$
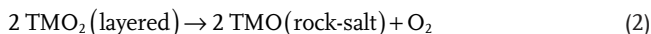
Because the Ni content of NCM CAMs strongly affects the crystal lattice stability and determines the degree of delithiation (for a given upper COV), O_2 evolution, and thus also CO_2/CO evolution, is shifted to lower cell potentials with increasing Ni content, leading to accelerated degradation.[219,220] Complementary results were obtained by Bak et al.[226] via combined synchrotron-based (time-resolved) XRD and mass spectroscopy. The oxygen release from various NCMs was further studied by Jung et al.,[91,219,220] clearly showing enhanced O_2 evolution with increasing Ni content. Apparently, there is a correlation between the oxygen release and the H2–H3 phase transformation, occurring in Ni-rich NCM CAMs at potentials above 4.1 V. Consistent results were also reported for the pure Ni endmember LNO.[213] We also note that O_2 evolution during both charging and discharging has been confirmed recently by DEMS measurements conducted on all-solid-state battery cells.[227]

For Li-rich layered oxides, the O_2 evolution usually occurs at high potentials.[101,219,220] During initial high-voltage charging up to 4.5–4.6 V vs Li^+/Li of HE-NCM CAMs, Li_2MnO_3-like domains are supposed to be activated by extraction of Li and O atoms from the lattice.[228] Using DEMS, Castel et al.[66]

demonstrated for $cLi_2MnO_3\cdot[1-c]LiTMO_2$ materials cycled in half-cells between 2.0 and 5.0 V that O_2 evolves above 4.7 V irrespective of the current rate, whereas CO_2 can already be detected above 3.7 V at low current rate. It is explained that the oxygen that is extracted from the Li_2MnO_3-like domains together with lithium is first accumulated in the form of Li_2O at the electrode–electrolyte interface.[229] The oxygen from such species is supposed to further react with electrolyte components/derivatives to form oxygen-rich "intermediates," such as peroxo radicals.[230] The systematic evolution observed near 4.7 V suggests that these "intermediates" further decompose, thereby leading to O_2 and CO_2 release from the interface. Lanz et al.[80] completed those measurements by a combination of DEMS, in situ pressure, and in situ temperature experiments on HE-NCM CAMs in full-cells. At the beginning of the charging process, they observed an internal pressure increase, presumably due to SEI formation on the graphite electrode and electrolyte decomposition on both electrodes, which, according to the DEMS, results in formation of H_2, C_2H_4, and CO_2. An accelerated increase in internal pressure at about 4.4 V was ascribed to oxygen release. The further increase in internal pressure above 4.6 V was attributed to strong oxidative decomposition of the electrolyte at high potentials. Unlike all other processes, the latter was also observed during the subsequent cycles.

5. Summary and Perspective

The intense battery research performed in recent years at KIT helped to contribute to better understanding of the mechanisms of formation and fatigue of layered transition metal oxides, in particular Ni-rich NCM and Li-rich HE-NCM CAMs. The characteristic process of formation of these materials and the fatigue mechanisms have been fundamentally characterized and the effect of chemical composition on cell chemistry, electrochemistry, and cycling stability addressed on different length scales using an arsenal of advanced analytical techniques. Among others, it was demonstrated that especially the properties of Ni-rich NCMs show strong correlations with those of $LiNiO_2$ (e.g., in terms of crystallographic changes and phase transformation behavior, eventually leading to material fatigue). The findings indicate the importance of electronic mixing in the nickel–oxygen states with respect to the stability of the crystal lattice, especially for high-energy-density applications, requiring high degrees of delithiation (>80%). Future research should clearly be focused on enhancing the electronic stability of materials to better protect them from, e.g., lattice oxygen loss. Several strategies aiming at improving the performance and stability of Ni-rich NCM CAMs are currently pursued. The most promising approaches are certainly: i) doping and ii) surface modification, as well as iii) implementing concentration gradients. Bulk doping seems to be a viable strategy to enhance both the cycling performance and structural stability.[57,231–233] Aluminum is a prime example of how partial substitution can dramatically improve the thermal stability of NCMs.[57,233–235] Promising dopants are Mg,[233,236–238] Ti,[231,239] Mo,[240] Nb,[241] Zr,[242] and Na[243]; they potentially increase the performance (presumably) due to stronger bonding with oxygen as compared

to Ni[244] and lower Li/Ni mixing.[238] Improvements in performance can also be achieved by anionic fluorine doping.[245] Furthermore, targeted protection through surface coating seems to be a promising approach to counteract electrolyte decomposition and formation of rock-salt-type or spinel phases. The longevity of cells using high-Ni NCM CAMs is found to be greatly improved by the presence of surface oxide[246–251] or phosphate coatings.[252–256] Also, molecular surface functionalization using organophosphates can apparently successfully reduce transition-metal dissolution, thereby positively affecting the cell cyclability.[257] Since there are indications for a more severe surface reconstruction along Li transport channels in NCM,[176] protective coatings applied on specific crystal orientations might be superior over others. Another alternative approach is the synthesis of compositionally graded NCM particles with Mn-rich shell and Ni-rich core.[258–262]

Regarding HE-NCMs, the presented work contributed to a more complete description of the pristine material's complex real structure by a sophisticated evaluation of the weak superstructure reflections. A fine and regular distribution of platelet-shaped Li_2MnO_3-like nanodomains with a high degree of stacking faults, coherently embedded within the NCM host matrix, is beneficial to achieve large discharge capacities by enabling (reversible) oxygen redox contribution to the charge compensation mechanism. Nanotwinning of rhombohedral domains during continuous cycling as a kind of intermediate structural modification toward a spinel-like phase (eventually forming with long-term cycling), represents a novel approach to explain the degradation mechanism of HE-NCMs. These results directed the focus of a proceeding research project on HE-NCM CAMs at KIT (restoration of a pristine-like state from cycled samples by thermal annealing), revealing that the structural/electronic changes occurring in the initial formation cycle are at least partially reversible. Furthermore, by profound investigations into lithium/oxygen incorporation and microstructural evolution during synthesis of Li-rich layered oxides, recently more insights into the degradation mechanism (that involves lithium and oxygen loss and an accompanied transition to a spinel-like phase) were gained,[263] which might point to future strategies to further improve the long-term stability of such CAMs.

Conflict of Interest

The authors declare no conflict of interest.

[1] F. Schipper, E. M. Erickson, C. Erk, J.-Y. Shin, F. F. Chesneau, D. Aurbach, *J. Electrochem. Soc.* **2017**, *164*, A6220.
[2] C. Julien, A. Mauger, K. Zaghib, H. Groult, *Materials* **2016**, *9*, 595.
[3] C. M. Julien, A. Mauger, K. Zaghib, H. Groult, *Inorganics* **2014**, *2*, 132.
[4] X. Yu, E. Hu, S. Bak, Y.-N. Zhou, X.-Q. Yang, *Chin. Phys. B* **2016**, *25*, 018205.
[5] J. Xu, F. Lin, M. M. Doeff, W. Tong, *J. Mater. Chem. A* **2017**, *5*, 874.
[6] L. Wang, J. Li, X. He, W. Pu, C. Wan, C. Jiang, *J. Solid State Electrochem.* **2009**, *13*, 1157.
[7] S.-T. Myung, F. Maglia, K.-J. Park, C. S. Yoon, P. Lamp, S.-J. Kim, Y.-K. Sun, *ACS Energy Lett.* **2017**, *2*, 196.
[8] J. Kasnatscheew, M. Evertz, R. Kloepsch, B. Streipert, R. Wagner, I. Cekic Laskovic, M. Winter, *Energy Technol.* **2017**, *5*, 1670.
[9] W. Liu, P. Oh, X. Liu, M.-J. Lee, W. Cho, S. Chae, Y. Kim, J. Cho, *Angew. Chem., Int. Ed.* **2015**, *54*, 4440.
[10] P. Rozier, J. M. Tarascon, *J. Electrochem. Soc.* **2015**, *162*, A2490.
[11] C. Ghanty, P. P. Dahiya, K. Sahoo, S. Basu, S. B. Majumder, *Rev. Adv. Sci. Eng.* **2016**, *5*, 65.
[12] J. Yan, X. Liu, B. Li, *RSC Adv.* **2014**, *4*, 63268.
[13] P. K. Nayak, E. M. Erickson, F. Schipper, T. R. Penki, N. Munichandraiah, P. Adelhelm, H. Sclar, F. Amalraj, B. Markovsky, D. Aurbach, *Adv. Energy Mater.* **2018**, *8*, 1702397.
[14] Y. Zhang, Y. Li, X. Xia, X. Wang, C. Gu, J. Tu, *Sci. China Technol. Sci.* **2015**, *58*, 1809.
[15] H. Yu, H. Zhou, *J. Phys. Chem. Lett.* **2013**, *4*, 1268.
[16] J. R. Croy, M. Balasubramanian, K. G. Gallagher, A. K. Burrell, *Acc. Chem. Res.* **2015**, *48*, 2813.
[17] K. Ishidzu, Y. Oka, T. Nakamura, *Solid State Ionics* **2016**, *288*, 176.
[18] H.-J. Noh, S. Youn, C. S. Yoon, Y.-K. Sun, *J. Power Sources* **2013**, *233*, 121.
[19] R. Wolf, R. Hoppe, *Z. Anorg. Allg. Chem.* **1989**, *568*, 147.
[20] W. Scheld, R. Hoppe, *Z. Anorg. Allg. Chem.* **1989**, *568*, 151.
[21] G. Amatucci, *Solid State Ionics* **1996**, *83*, 167.
[22] J. Akimoto, Y. Gotoh, Y. Oosawa, *J. Solid State Chem.* **1998**, *141*, 298.
[23] Y. Oh, J. Lee, B. Kim, B. Park, *Electron. Mater. Lett.* **2008**, *4*, 9.
[24] Y.-I. Jang, N. J. Dudney, D. A. Blom, L. F. Allard, *J. Electrochem. Soc.* **2002**, *149*, A1442.
[25] B. L. Ellis, K. T. Lee, L. F. Nazar, *Chem. Mater.* **2010**, *22*, 691.
[26] T. Ohzuku, A. Ueda, M. Nagayama, *J. Electrochem. Soc.* **1993**, *140*, 1862.
[27] W. Ebner, D. Fouchard, L. Xie, *Solid State Ionics* **1994**, *69*, 238.
[28] A. O. Kondrakov, A. Schmidt, J. Xu, H. Geßwein, R. Mönig, P. Hartmann, H. Sommer, T. Brezesinski, J. Janek, *J. Phys. Chem. C* **2017**, *121*, 3286.
[29] X. Zhao, Q.-C. Zhuang, C. Wu, K. Wu, J.-M. Xu, M.-Y. Zhang, X.-L. Sun, *J. Electrochem. Soc.* **2015**, *162*, A2770.
[30] C. H. Chen, J. Liu, M. E. Stoll, G. Henriksen, D. R. Vissers, K. Amine, *J. Power Sources* **2004**, *128*, 278.
[31] I. Belharouak, W. Lu, D. Vissers, K. Amine, *Electrochem. Commun.* **2006**, *8*, 329.
[32] I. Rossouw, M. M. Thackeray, *Patent No. 5166012* **2006**.
[33] M. M. Thackeray, M. H. Rossouw, A. de Kock, A. P. de la Harpe, R. J. Gummow, K. Pearce, D. C. Liles, *J. Power Sources* **1993**, *43*, 289.
[34] M. M. Thackeray, S.-H. Kang, C. S. Johnson, J. T. Vaughey, R. Benedek, S. A. Hackney, *J. Mater. Chem.* **2007**, *17*, 3112.
[35] S. Cui, Y. Wei, T. Liu, W. Deng, Z. Hu, Y. Su, H. Li, M. Li, H. Guo, Y. Duan, W. Wang, M. Rao, J. Zheng, X. Wang, F. Pan, *Adv. Energy Mater.* **2016**, *6*, 1501309.
[36] P. J. Phillips, J. Bareño, Y. Li, D. P. Abraham, R. F. Klie, *Adv. Energy Mater.* **2015**, *5*, 1501252.
[37] H. Deng, I. Belharouak, Y.-K. Sun, K. Amine, *J. Mater. Chem.* **2009**, *19*, 4510.

**ADVANCED
SCIENCE NEWS**

www.advancedsciencenews.com

**ADVANCED
MATERIALS**

www.advmat.de

[38] D. Ye, G. Zeng, K. Nogita, K. Ozawa, M. Hankel, D. J. Searles, L. Wang, *Adv. Funct. Mater.* **2015**, *25*, 7488.

[39] J. Zeng, Y. Cui, D. Qu, Q. Zhang, J. Wu, X. Zhu, Z. Li, X. Zhang, *ACS Appl. Mater. Interfaces* **2016**, *8*, 26082.

[40] J.-S. Kim, C. S. Johnson, M. M. Thackeray, *Electrochem. Commun.* **2002**, *4*, 205.

[41] J.-S. Kim, C. S. Johnson, J. T. Vaughey, M. M. Thackeray, S. A. Hackney, W. Yoon, C. P. Grey, *Chem. Mater.* **2004**, *16*, 1996.

[42] M. M. Thackeray, C. S. Johnson, J. T. Vaughey, N. Li, S. A. Hackney, *J. Mater. Chem.* **2005**, *15*, 2257.

[43] T. Ohzuku, Y. Makimura, *Chem. Lett.* **2001**, *30*, 642.

[44] M. Armand, J. M. Tarascon, *Nature* **2008**, *451*, 652.

[45] Z.-D. Huang, X.-M. Liu, S.-W. Oh, B. Zhang, P.-C. Ma, J.-K. Kim, *J. Mater. Chem.* **2011**, *21*, 10777.

[46] C. Venkateswara Rao, A. Leela Mohana Reddy, Y. Ishikawa, P. M. Ajayan, *ACS Appl. Mater. Interfaces* **2011**, *3*, 2966.

[47] N. Yabuuchi, Y. Makimura, T. Ohzuku, *J. Electrochem. Soc.* **2007**, *154*, A314.

[48] M. M. Thackeray, S.-H. Kang, C. S. Johnson, J. T. Vaughey, S. A. Hackney, *Electrochem. Commun.* **2006**, *8*, 1531.

[49] Z. Lu, D. D. MacNeil, J. R. Dahn, *Electrochem. Solid-State Lett.* **2001**, *4*, A191.

[50] A. R. Armstrong, M. Holzapfel, P. Novák, C. S. Johnson, S.-H. Kang, M. M. Thackeray, P. G. Bruce, *J. Am. Chem. Soc.* **2006**, *128*, 8694.

[51] C. S. Johnson, N. Li, C. Lefief, J. T. Vaughey, M. M. Thackeray, *Chem. Mater.* **2008**, *20*, 6095.

[52] M. Gu, I. Belharouak, J. Zheng, H. Wu, J. Xiao, A. Genc, K. Amine, S. Thevuthasan, D. R. Baer, J.-G. Zhang, N. D. Browning, J. Liu, C. Wang, *ACS Nano* **2013**, *7*, 760.

[53] S.-M. Bak, E. Hu, Y. Zhou, X. Yu, S. D. Senanayake, S.-J. Cho, K.-B. Kim, K. Y. Chung, X.-Q. Yang, K.-W. Nam, *ACS Appl. Mater. Interfaces* **2014**, *6*, 22594.

[54] B. B. Berkes, A. Jozwiuk, H. Sommer, T. Brezesinski, J. Janek, *Electrochem. Commun.* **2015**, *60*, 64.

[55] B. B. Berkes, A. Jozwiuk, M. Vračar, H. Sommer, T. Brezesinski, J. Janek, *Anal. Chem.* **2015**, *87*, 5878.

[56] B. B. Berkes, A. Schiele, H. Sommer, T. Brezesinski, J. Janek, *J. Solid State Electrochem.* **2016**, *20*, 2961.

[57] D. Aurbach, O. Srur-Lavi, C. Ghanty, M. Dixit, O. Haik, M. Talianker, Y. Grinblat, N. Leifer, R. Lavi, D. T. Major, *J. Electrochem. Soc.* **2015**, *162*, A1014.

[58] X. Bie, F. Du, Y. Wang, K. Zhu, H. Ehrenberg, K. Nikolowski, C. Wang, G. Chen, Y. Wei, *Electrochim. Acta* **2013**, *97*, 357.

[59] X. Xiong, Z. Wang, P. Yue, H. Guo, F. Wu, J. Wang, X. Li, *J. Power Sources* **2013**, *222*, 318.

[60] S.-G. Woo, J.-H. Han, K. J. Kim, J.-H. Kim, J.-S. Yu, Y.-J. Kim, *Electrochim. Acta* **2015**, *153*, 115.

[61] L. de Biasi, A. O. Kondrakov, H. Geßwein, T. Brezesinski, P. Hartmann, J. Janek, *J. Phys. Chem. C* **2017**, *121*, 26163.

[62] A. O. Kondrakov, H. Geßwein, K. Galdina, L. de Biasi, V. Meded, E. O. Filatova, G. Schumacher, W. Wenzel, P. Hartmann, T. Brezesinski, J. Janek, *J. Phys. Chem. C* **2017**, *121*, 24381.

[63] J. Li, L. E. Downie, L. Ma, W. Qiu, J. R. Dahn, *J. Electrochem. Soc.* **2015**, *162*, A1401.

[64] T. A. Arunkumar, Y. Wu, A. Manthiram, *Chem. Mater.* **2007**, *19*, 3067.

[65] N. Tran, L. Croguennec, M. Ménétrier, F. Weill, P. Biensan, C. Jordy, C. Delmas, *Chem. Mater.* **2008**, *20*, 4815.

[66] E. Castel, E. J. Berg, M. El Kazzi, P. Novák, C. Villevieille, *Chem. Mater.* **2014**, *26*, 5051.

[67] C. S. Johnson, N. Li, C. Lefief, M. M. Thackeray, *Electrochem. Commun.* **2007**, *9*, 787.

[68] T. Ohzuku, M. Nagayama, K. Tsuji, K. Ariyoshi, *J. Mater. Chem.* **2011**, *21*, 10179.

[69] M. Sathiya, G. Rousse, K. Ramesha, C. P. Laisa, H. Vezin, M. T. Sougrati, M. L. Doublet, D. Foix, D. Gonbeau, W. Walker, A. S. Prakash, M. Ben Hassine, L. Dupont, J. M. Tarascon, *Nat. Mater.* **2013**, *12*, 827.

[70] F. Dogan, B. R. Long, J. R. Croy, K. G. Gallagher, H. Iddir, J. T. Russell, M. Balasubramanian, B. Key, *J. Am. Chem. Soc.* **2015**, *137*, 2328.

[71] L. Riekehr, J. Liu, B. Schwarz, F. Sigel, I. Kerkamm, Y. Xia, H. Ehrenberg, *J. Power Sources* **2016**, *325*, 391.

[72] A. Boulineau, L. Simonin, J.-F. Colin, E. Canévet, L. Daniel, S. Patoux, *Chem. Mater.* **2012**, *24*, 3558.

[73] B. Song, Z. Liu, M. O. Lai, L. Lu, *Phys. Chem. Chem. Phys.* **2012**, *14*, 12875.

[74] D. Mohanty, S. Kalnaus, R. A. Meisner, K. J. Rhodes, J. Li, E. A. Payzant, D. L. Wood, C. Daniel, *J. Power Sources* **2013**, *229*, 239.

[75] Z. Q. Deng, A. Manthiram, *J. Phys. Chem. C* **2011**, *115*, 7097.

[76] J. Hong, D.-H. Seo, S.-W. Kim, H. Gwon, S.-T. Oh, K. Kang, *J. Mater. Chem.* **2010**, *20*, 10179.

[77] A. Ito, D. Li, Y. Sato, M. Arao, M. Watanabe, M. Hatano, H. Horie, Y. Ohsawa, *J. Power Sources* **2010**, *195*, 567.

[78] K. A. Jarvis, C. C. Wang, A. Manthiram, P. J. Ferreira, *J. Mater. Chem. A* **2014**, *2*, 1353.

[79] P. Lanz, C. Villevieille, P. Novák, *Electrochim. Acta* **2014**, *130*, 206.

[80] P. Lanz, H. Sommer, M. Schulz-Dobrick, P. Novák, *Electrochim. Acta* **2013**, *93*, 114.

[81] W. He, J. Qian, Y. Cao, X. Ai, H. Yang, *RSC Adv.* **2012**, *2*, 3423.

[82] J. Jiang, J. R. Dahn, *Electrochim. Acta* **2006**, *51*, 3413.

[83] J. Vetter, P. Novák, M. R. Wagner, C. Veit, K.-C. Möller, J. O. Besenhard, M. Winter, M. Wohlfahrt-Mehrens, C. Vogler, A. Hammouche, *J. Power Sources* **2005**, *147*, 269.

[84] M. Wohlfahrt-Mehrens, C. Vogler, J. Garche, *J. Power Sources* **2004**, *127*, 58.

[85] A. Barré, B. Deguilhem, S. Grolleau, M. Gérard, F. Suard, D. Riu, *J. Power Sources* **2013**, *241*, 680.

[86] C. R. Birkl, M. R. Roberts, E. McTurk, P. G. Bruce, D. A. Howey, *J. Power Sources* **2017**, *341*, 373.

[87] M. Broussely, S. Herreyre, P. Biensan, P. Kasztejna, K. Nechev, R. J. Staniewicz, *J. Power Sources* **2001**, *97–98*, 13.

[88] P. Keil, A. Jossen, *J. Electrochem. Soc.* **2017**, *164*, A6066.

[89] C. Hafner, T. Bernthaler, V. Knoblauch, G. Schneider, *Pract. Metallogr.* **2012**, *49*, 75.

[90] G. Sun, T. Sui, B. Song, H. Zheng, L. Lu, A. M. Korsunsky, *Extreme Mech. Lett.* **2016**, *9*, 449.

[91] S.-K. Jung, H. Gwon, J. Hong, K.-Y. Park, D.-H. Seo, H. Kim, J. Hyun, W. Yang, K. Kang, *Adv. Energy Mater.* **2014**, *4*, 1300787.

[92] R. Koerver, W. Zhang, L. de Biasi, S. Schweidler, A. O. Kondrakov, S. Kolling, T. Brezesinski, P. Hartmann, W. G. Zeier, J. Janek, *Energy Environ. Sci.* **2018**, *11*, 2142.

[93] R. Jung, R. Morasch, P. Karayaylali, K. Phillips, F. Maglia, C. Stinner, Y. Shao-Horn, H. A. Gasteiger, *J. Electrochem. Soc.* **2018**, *165*, A132.

[94] D. Aurbach, *J. Power Sources* **2000**, *89*, 206.

[95] J. A. Gilbert, I. A. Shkrob, D. P. Abraham, *J. Electrochem. Soc.* **2017**, *164*, A389.

[96] J. Wandt, A. Freiberg, R. Thomas, Y. Gorlin, A. Siebel, R. Jung, H. A. Gasteiger, M. Tromp, *J. Mater. Chem. A* **2016**, *4*, 18300.

[97] H. Zheng, Q. Sun, G. Liu, X. Song, V. S. Battaglia, *J. Power Sources* **2012**, *207*, 134.

[98] J. Kim, H. Ma, H. Cha, H. Lee, J. Sung, M. Seo, P. Oh, M. Park, J. Cho, *Energy Environ. Sci.* **2018**, *11*, 1449.

[99] M.-T. F. Rodrigues, K. Kalaga, S. E. Trask, I. A. Shkrob, D. P. Abraham, *J. Electrochem. Soc.* **2018**, *165*, A1697.

[100] H. Wang, E. Rus, T. Sakuraba, J. Kikuchi, Y. Kiya, H. D. Abruña, *Anal. Chem.* **2014**, *86*, 6197.

[101] R. Jung, P. Strobl, F. Maglia, C. Stinner, H. A. Gasteiger, *J. Electrochem. Soc.* **2018**, *165*, A2869.

[102] A. Schiele, T. Hatsukade, B. B. Berkes, P. Hartmann, T. Brezesinski, J. Janek, *Anal. Chem.* **2017**, *89*, 8122.

[103] S. Schweidler, L. de Biasi, A. Schiele, P. Hartmann, T. Brezesinski, J. Janek, *J. Phys. Chem. C* **2018**, *122*, 8829.

[104] C. Ghanty, B. Markovsky, E. M. Erickson, M. Talianker, O. Haik, Y. Tal-Yossef, A. Mor, D. Aurbach, J. Lampert, A. Volkov, J.-Y. Shin, A. Garsuch, F. F. Chesneau, C. Erk, *ChemElectroChem* **2015**, *2*, 1479.

[105] N. Yabuuchi, Y. Koyama, N. Nakayama, T. Ohzuku, *J. Electrochem. Soc.* **2005**, *152*, A1434.

[106] W. Li, J. N. Reimers, J. R. Dahn, *Solid State Ionics* **1993**, *67*, 123.

[107] C. Delmas, C. Fouassier, P. Hagenmuller, *Physica B+C* **1980**, *99*, 81.

[108] Y. Koyama, N. Yabuuchi, I. Tanaka, H. Adachi, T. Ohzuku, *J. Electrochem. Soc.* **2004**, *151*, A1545.

[109] T. A. Hewston, B. L. Chamberland, *J. Phys. Chem. Solids* **1987**, *48*, 97.

[110] M. Wang, A. Navrotsky, *J. Solid State Chem.* **2005**, *178*, 1230.

[111] M. Obrovac, *Solid State Ionics* **1998**, *112*, 9.

[112] Y. Song, X. Zhao, C. Wang, H. Bi, J. Zhang, S. Li, M. Wang, R. Che, *J. Mater. Chem. A* **2017**, *5*, 11214.

[113] M. H. Rossouw, A. de Kock, I. A. de Picciotto, M. M. Thackeray, W. I. F. David, R. M. Ibberson, *Mater. Res. Bull.* **1990**, *25*, 173.

[114] M. M. J. Treacy, J. M. Newsam, M. W. Deem, *Proc. R. Soc. London, Ser. A* **1991**, *433*, 499.

[115] B.-C. Park, H. J. Bang, C. S. Yoon, S.-T. Myung, J. Prakash, Y.-K. Sun, *J. Electrochem. Soc.* **2007**, *154*, A520.

[116] S.-C. Yin, Y.-H. Rho, I. Swainson, L. F. Nazar, *Chem. Mater.* **2006**, *18*, 1901.

[117] H. Yu, H. Kim, Y. Wang, P. He, D. Asakura, Y. Nakamura, H. Zhou, *Phys. Chem. Chem. Phys.* **2012**, *14*, 6584.

[118] C. S. Johnson, J.-S. Kim, C. Lefief, N. Li, J. T. Vaughey, M. M. Thackeray, *Electrochem. Commun.* **2004**, *6*, 1085.

[119] K. A. Jarvis, Z. Deng, L. F. Allard, A. Manthiram, P. J. Ferreira, *J. Mater. Chem.* **2012**, *22*, 11550.

[120] C. H. Lei, J. Bareño, J. G. Wen, I. Petrov, S.-H. Kang, D. P. Abraham, *J. Power Sources* **2008**, *178*, 422.

[121] J. Bareño, M. Balasubramanian, S. H. Kang, J. G. Wen, C. H. Lei, S. V. Pol, I. Petrov, D. P. Abraham, *Chem. Mater.* **2011**, *23*, 2039.

[122] J. Bréger, M. Jiang, N. Dupré, Y. S. Meng, Y. Shao-Horn, G. Ceder, C. P. Grey, *J. Solid State Chem.* **2005**, *178*, 2575.

[123] Y. S. Meng, G. Ceder, C. P. Grey, W.-S. Yoon, M. Jiang, J. Bréger, Y. Shao-Horn, *Chem. Mater.* **2005**, *17*, 2386.

[124] J. G. Wen, J. Bareño, C. H. Lei, S. H. Kang, M. Balasubramanian, I. Petrov, D. P. Abraham, *Solid State Ionics* **2011**, *182*, 98.

[125] K. A. Jarvis, Z. Deng, L. F. Allard, A. Manthiram, P. J. Ferreira, *Chem. Mater.* **2011**, *23*, 3614.

[126] J. R. Dahn, E. W. Fuller, M. Obrovac, U. Von Sacken, *Solid State Ionics* **1994**, *69*, 265.

[127] W.-S. Yoon, K. Y. Chung, J. McBreen, X.-Q. Yang, *Electrochem. Commun.* **2006**, *8*, 1257.

[128] L. Wu, K.-W. Nam, X. Wang, Y. Zhou, J.-C. Zheng, X.-Q. Yang, Y. Zhu, *Chem. Mater.* **2011**, *23*, 3953.

[129] R. Hausbrand, G. Cherkashinin, H. Ehrenberg, M. Gröting, K. Albe, C. Hess, W. Jaegermann, *Mater. Sci. Eng., B* **2015**, *192*, 3.

[130] H.-R. Kim, S.-G. Woo, J.-H. Kim, W. Cho, Y.-J. Kim, *J. Electroanal. Chem.* **2016**, *782*, 168.

[131] I. Buchberger, S. Seidlmayer, A. Pokharel, M. Piana, J. Hattendorff, P. Kudejova, R. Gilles, H. A. Gasteiger, *J. Electrochem. Soc.* **2015**, *162*, A2737.

[132] J. Li, R. Petibon, S. Glazier, N. Sharma, W. K. Pang, V. K. Peterson, J. R. Dahn, *Electrochim. Acta* **2015**, *180*, 234.

[133] K. Min, K. Kim, C. Jung, S.-W. Seo, Y. Y. Song, H. S. Lee, J. Shin, E. Cho, *J. Power Sources* **2016**, *315*, 111.

[134] F. Strauss, T. Bartsch, L. de Biasi, A.-Y. Kim, J. Janek, P. Hartmann, T. Brezesinski, *ACS Energy Lett.* **2018**, *3*, 992.

[135] L. de Biasi, G. Lieser, J. Rana, S. Indris, C. Dräger, S. Glatthaar, R. Mönig, H. Ehrenberg, G. Schumacher, J. R. Binder, H. Geßwein, *CrystEngComm* **2015**, *17*, 6163.

[136] W. Lee, S. Muhammad, T. Kim, H. Kim, E. Lee, M. Jeong, S. Son, J.-H. Ryou, W.-S. Yoon, *Adv. Energy Mater.* **2018**, *8*, 1701788.

[137] H. Arai, S. Okada, H. Ohtsuka, M. Ichimura, J. Yamaki, *Solid State Ionics* **1995**, *80*, 261.

[138] A. Hirano, R. Kanno, Y. Kawamoto, Y. Takeda, K. Yamaura, M. Takano, K. Ohyama, M. Ohashi, Y. Yamaguchi, *Solid State Ionics* **1995**, *78*, 123.

[139] H. Li, N. Zhang, J. Li, J. R. Dahn, *J. Electrochem. Soc.* **2018**, *165*, A2985.

[140] M. Bianchini, M. Roca-Ayats, P. Hartmann, T. Brezesinski, J. Janek, *Angew. Chem., Int. Ed.* **2018**, https://doi.org/10.1002/anie.201812472.

[141] H. Arai, S. Okada, Y. Sakurai, J. Yamaki, *Solid State Ionics* **1997**, *95*, 275.

[142] H. Arai, S. Okada, Y. Sakurai, J. Yamaki, *J. Electrochem. Soc.* **1997**, *144*, 3117.

[143] U.-H. Kim, D.-W. Jun, K.-J. Park, Q. Zhang, P. Kaghazchi, D. Aurbach, D. T. Major, G. Goobes, M. Dixit, N. Leifer, C. M. Wang, P. Yan, D. Ahn, K.-H. Kim, C. S. Yoon, Y.-K. Sun, *Energy Environ. Sci.* **2018**, *11*, 1271.

[144] H.-H. Ryu, K.-J. Park, C. S. Yoon, Y.-K. Sun, *Chem. Mater.* **2018**, *30*, 1155.

[145] H.-H. Sun, A. Manthiram, *Chem. Mater.* **2017**, *29*, 8486.

[146] D.-W. Jun, C. S. Yoon, U.-H. Kim, Y.-K. Sun, *Chem. Mater.* **2017**, *29*, 5048.

[147] S.-G. Woo, J.-H. Kim, H.-R. Kim, W. Cho, J.-S. Yu, *J. Electroanal. Chem.* **2017**, *799*, 315.

[148] A. Van der Ven, M. K. Aydinol, G. Ceder, G. Kresse, J. Hafner, *Phys. Rev. B* **1998**, *58*, 2975.

[149] X. Zhang, A. Mauger, Q. Lu, H. Groult, L. Perrigaud, F. Gendron, C. M. Julien, *Electrochim. Acta* **2010**, *55*, 6440.

[150] Y. W. Tsai, B. J. Hwang, G. Ceder, H. S. Sheu, D. G. Liu, J. F. Lee, *Chem. Mater.* **2005**, *17*, 3191.

[151] K. Kleiner, J. Melke, M. Merz, P. Jakes, P. Nagel, S. Schuppler, V. Liebau, H. Ehrenberg, *ACS Appl. Mater. Interfaces* **2015**, *7*, 19589.

[152] D. Y. W. Yu, K. Yanagida, Y. Kato, H. Nakamura, *J. Electrochem. Soc.* **2009**, *156*, A417.

[153] Z. Lu, J. R. Dahn, *J. Electrochem. Soc.* **2002**, *149*, A815.

[154] R. Wang, X. He, L. He, F. Wang, R. Xiao, L. Gu, H. Li, L. Chen, *Adv. Energy Mater.* **2013**, *3*, 1358.

[155] B. Strehle, K. Kleiner, R. Jung, F. Chesneau, M. Mendez, H. A. Gasteiger, M. Piana, *J. Electrochem. Soc.* **2017**, *164*, A400.

[156] K. Kleiner, B. Strehle, A. R. Baker, S. J. Day, C. C. Tang, I. Buchberger, F.-F. Chesneau, H. A. Gasteiger, M. Piana, *Chem. Mater.* **2018**, *30*, 3656.

[157] T. Ohzuku, A. Ueda, *Solid State Ionics* **1994**, *69*, 201.

[158] J.-M. Kim, H.-T. Chung, *Electrochim. Acta* **2004**, *49*, 937.

[159] G. Assat, D. Foix, C. Delacourt, A. Iadecola, R. Dedryvère, J. M. Tarascon, *Nat. Commun.* **2017**, *8*, 2219.

[160] E. Salager, V. Sarou-Kanian, M. Sathiya, M. Tang, J.-B. Leriche, P. Melin, Z. Wang, H. Vezin, C. Bessada, M. Deschamps, J.-M. Tarascon, *Chem. Mater.* **2014**, *26*, 7009.

[161] T. Teufl, B. Strehle, P. Müller, H. A. Gasteiger, M. A. Mendez, *J. Electrochem. Soc.* **2018**, *165*, A2718.

[162] J. R. Croy, K. G. Gallagher, M. Balasubramanian, Z. Chen, Y. Ren, D. Kim, S.-H. Kang, D. W. Dees, M. M. Thackeray, *J. Phys. Chem. C* **2013**, *117*, 6525.

[163] A. D. Robertson, P. G. Bruce, *Chem. Mater.* **2003**, *15*, 1984.

[164] A. Singer, S. Hy, M. Zhang, D. Cela, C. Fang, B. Qiu, Y. Xia, Z. Liu, N. Hua, J. Wingert, H. Liu, M. Sprung, A. V. Zozulya, E. Maxey, Y. S. Meng, O. G. Shpyrko, *Nat. Energy* **2018**, *3*, 641.

[165] L. Riekehr, J. Liu, B. Schwarz, F. Sigel, I. Kerkamm, Y. Xia, H. Ehrenberg, *J. Power Sources* **2016**, *306*, 135.

[166] K. Kleiner, D. Dixon, P. Jakes, J. Melke, M. Yavuz, C. Roth, K. Nikolowski, V. Liebau, H. Ehrenberg, *J. Power Sources* **2015**, *273*, 70.

[167] M. Herklotz, F. Scheiba, M. Hinterstein, K. Nikolowski, M. Knapp, A.-C. Dippel, L. Giebeler, J. Eckert, H. Ehrenberg, *J. Appl. Crystallogr.* **2013**, *46*, 1117.

[168] W. E. Gent, Y. Li, S. Ahn, J. Lim, Y. Liu, A. M. Wise, C. B. Gopal, D. N. Mueller, R. Davis, J. N. Weker, J.-H. Park, S.-K. Doo, W. C. Chueh, *Adv. Mater.* **2016**, *28*, 6631.

[169] H. Liu, M. Wolf, K. Karki, Y.-S. Yu, E. A. Stach, J. Cabana, K. W. Chapman, P. J. Chupas, *Nano Lett.* **2017**, *17*, 3452.

[170] C. S. Yoon, M. H. Choi, B.-B. Lim, E.-J. Lee, Y.-K. Sun, *J. Electrochem. Soc.* **2015**, *162*, A2483.

[171] A. Boulineau, L. Simonin, J.-F. Colin, C. Bourbon, S. Patoux, *Nano Lett.* **2013**, *13*, 3857.

[172] S. Hwang, W. Chang, S. M. Kim, D. Su, D. H. Kim, J. Y. Lee, K. Y. Chung, E. A. Stach, *Chem. Mater.* **2014**, *26*, 1084.

[173] S. Zheng, R. Huang, Y. Makimura, Y. Ukyo, C. A. Fisher, T. Hirayama, Y. Ikuhara, *J. Electrochem. Soc.* **2011**, *158*, A357.

[174] Y. Makimura, S. Zheng, Y. Ikuhara, Y. Ukyo, *J. Electrochem. Soc.* **2012**, *159*, A1070.

[175] U.-H. Kim, S.-T. Myung, C. S. Yoon, Y.-K. Sun, *ACS Energy Lett.* **2017**, *2*, 1848.

[176] F. Lin, I. M. Markus, D. Nordlund, T.-C. Weng, M. D. Asta, H. L. Xin, M. M. Doeff, *Nat. Commun.* **2014**, *5*, 3529.

[177] K. Karki, Y. Huang, S. Hwang, A. D. Gamalski, M. S. Whittingham, G. Zhou, E. A. Stach, *ACS Appl. Mater. Interfaces* **2016**, *8*, 27762.

[178] D. Mohanty, K. Dahlberg, D. M. King, L. A. David, A. S. Sefat, D. L. Wood, C. Daniel, S. Dhar, V. Mahajan, M. Lee, F. Albano, *Sci. Rep.* **2016**, *6*, 26532.

[179] H. Zhang, F. Omenya, M. S. Whittingham, C. Wang, G. Zhou, *ACS Energy Lett.* **2017**, *2*, 2598.

[180] D. J. Miller, C. Proff, J. G. Wen, D. P. Abraham, J. Bareño, *Adv. Energy Mater.* **2013**, *3*, 1098.

[181] S. Watanabe, M. Kinoshita, T. Hosokawa, K. Morigaki, K. Nakura, *J. Power Sources* **2014**, *260*, 50.

[182] S. Kuze, D. du Boulay, N. Ishizawa, N. Kodama, M. Yamaga, B. Henderson, *J. Solid State Chem.* **2004**, *177*, 3505.

[183] W.-B. Hua, X.-D. Guo, Z. Zheng, Y.-J. Wang, B.-H. Zhong, B. Fang, J.-Z. Wang, S.-L. Chou, H. Liu, *J. Power Sources* **2015**, *275*, 200.

[184] Z. Yang, J. Lu, D. Bian, W. Zhang, X. Yang, J. Xia, G. Chen, H. Gu, G. Ma, *J. Power Sources* **2014**, *272*, 144.

[185] K. M. Shaju, P. G. Bruce, *Adv. Mater.* **2006**, *18*, 2330.

[186] P. Yan, J. Zheng, T. Chen, L. Luo, Y. Jiang, K. Wang, M. Sui, J.-G. Zhang, S. Zhang, C. Wang, *Nat. Commun.* **2018**, *9*, 2437.

[187] P. Yan, J. Zheng, M. Gu, J. Xiao, J.-G. Zhang, C.-M. Wang, *Nat. Commun.* **2017**, *8*, 14101.

[188] H. Zhang, F. Omenya, P. Yan, L. Luo, M. S. Whittingham, C. Wang, G. Zhou, *ACS Energy Lett.* **2017**, *2*, 2607.

[189] A. Ito, K. Shoda, Y. Sato, M. Hatano, H. Horie, Y. Ohsawa, *J. Power Sources* **2011**, *196*, 4785.

[190] B. Xu, C. R. Fell, M. Chi, Y. S. Meng, *Energy Environ. Sci.* **2011**, *4*, 2223.

[191] C. P. Grey, W.-S. Yoon, J. Reed, G. Ceder, *Electrochem. Solid-State Lett.* **2004**, *7*, A290.

[192] H. Koga, L. Croguennec, M. Ménétrier, K. Douhil, S. Belin, L. Bourgeois, E. Suard, F. Weill, C. Delmas, *J. Electrochem. Soc.* **2013**, *160*, A786.

[193] J. Reed, G. Ceder, *Chem. Rev.* **2004**, *104*, 4513.

[194] Y. S. Meng, M. E. Arroyo-De Dompablo, *Energy Environ. Sci.* **2009**, *2*, 589.

[195] G. Kobayashi, Y. Irii, F. Matsumoto, A. Ito, Y. Ohsawa, S. Yamamoto, Y. Cui, J.-Y. Son, Y. Sato, *J. Power Sources* **2016**, *303*, 250.

[196] N. Dannehl, S. O. Steinmüller, D. V. Szabó, F. Sigel, L. Esmezjan, U. Hasenkox, B. Schwarz, S. Indris, H. Ehrenberg, *ACS Appl. Mater. Interfaces* **2018**, *10*, 43131.

[197] Y. Wu, A. Manthiram, *Electrochem. Solid-State Lett.* **2006**, *9*, A221.

[198] X. Zhang, I. Belharouak, L. Li, Y. Lei, J. W. Elam, A. Nie, X. Chen, R. S. Yassar, R. L. Axelbaum, *Adv. Energy Mater.* **2013**, *3*, 1299.

[199] G. R. Li, X. Feng, Y. Ding, S. H. Ye, X. P. Gao, *Electrochim. Acta* **2012**, *78*, 308.

[200] J. Zheng, M. Gu, J. Xiao, B. J. Polzin, P. Yan, X. Chen, C. Wang, J.-G. Zhang, *Chem. Mater.* **2014**, *26*, 6320.

[201] S. Sun, Y. Yin, N. Wan, Q. Wu, X. Zhang, D. Pan, Y. Bai, X. Lu, *ChemSusChem* **2015**, *8*, 2544.

[202] P. K. Nayak, J. Grinblat, M. Levi, E. Levi, S. Kim, J. W. Choi, D. Aurbach, *Adv. Energy Mater.* **2016**, *6*, 1502398.

[203] B. Song, C. Zhou, H. Wang, H. Liu, Z. Liu, M. O. Lai, L. Lu, *J. Electrochem. Soc.* **2014**, *161*, A1723.

[204] D. Wang, Y. Huang, Z. Huo, L. Chen, *Electrochim. Acta* **2013**, *107*, 461.

[205] P. K. Nayak, J. Grinblat, E. Levi, M. Levi, B. Markovsky, D. Aurbach, *Phys. Chem. Chem. Phys.* **2017**, *19*, 6142.

[206] W. He, D. Yuan, J. Qian, X. Ai, H. Yang, Y. Cao, *J. Mater. Chem. A* **2013**, *1*, 11397.

[207] M. N. Ates, Q. Jia, A. Shah, A. Busnaina, S. Mukerjee, K. M. Abraham, *J. Electrochem. Soc.* **2014**, *161*, A290.

[208] L. Ming, B. Zhang, Y. Cao, J.-F. Zhang, C.-H. Wang, X.-W. Wang, H. Li, *Front. Chem.* **2018**, *6*, 76.

[209] B. Song, M. O. Lai, L. Lu, *Electrochim. Acta* **2012**, *80*, 187.

[210] S. Kang, H. Qin, Y. Fang, X. Li, Y. Wang, *Electrochim. Acta* **2014**, *144*, 22.

[211] H. Chen, Q. Hu, Z. Huang, Z. He, Z. Wang, H. Guo, X. Li, *Ceram. Int.* **2016**, *42*, 263.

[212] A. Schiele, B. Breitung, A. Mazilkin, S. Schweidler, J. Janek, S. Gumbel, S. Fleischmann, E. Burakowska-Meise, H. Sommer, T. Brezesinski, *ACS Omega* **2018**, *3*, 16706.

[213] L. de Biasi, A. Schiele, M. Roca-Ayats, G. Garcia Nino, T. Brezesinski, P. Hartmann, J. Janek, *ChemSusChem*, **2019**, https://doi.org/10.1002/cssc.201900032.

[214] A. Schiele, H. Sommer, T. Brezesinski, J. Janek, B. B. Berkes, in *Encyclopedia of Interfacial Chemistry: Surface Science and Electrochemistry* (Ed: K. Wandelt), Elsevier, Amsterdam, The Netherlands **2018**.

[215] B. Michalak, B. B. Berkes, H. Sommer, T. Bergfeldt, T. Brezesinski, J. Janek, *Anal. Chem.* **2016**, *88*, 2877.

[216] T. Hatsukade, A. Schiele, P. Hartmann, T. Brezesinski, J. Janek, *ACS Appl. Mater. Interfaces* **2018**, *10*, 38892.

[217] R. Imhof, *J. Electrochem. Soc.* **1999**, *146*, 1702.

[218] F. La Mantia, P. Novák, *Electrochem. Solid-State Lett.* **2008**, *11*, A84.

[219] R. Jung, M. Metzger, F. Maglia, C. Stinner, H. A. Gasteiger, *J. Electrochem. Soc.* **2017**, *164*, A1361.

[220] R. Jung, M. Metzger, F. Maglia, C. Stinner, H. A. Gasteiger, *J. Phys. Chem. Lett.* **2017**, *8*, 4820.

[221] R. Imhof, P. Novak, *J. Electrochem. Soc.* **1998**, *145*, 1081.

[222] R. Bernhard, S. Meini, H. A. Gasteiger, *J. Electrochem. Soc.* **2014**, *161*, A497.

[223] A. Schiele, B. Breitung, T. Hatsukade, B. B. Berkes, P. Hartmann, J. Janek, T. Brezesinski, *ACS Energy Lett.* **2017**, *2*, 2228.

[224] H. Ota, Y. Sakata, A. Inoue, S. Yamaguchi, *J. Electrochem. Soc.* **2004**, *151*, A1659.

1900985 (23 of 24)

**ADVANCED
SCIENCE NEWS**

www.advancedsciencenews.com

**ADVANCED
MATERIALS**

www.advmat.de

[225] A. Guéguen, D. Streich, M. He, M. Mendez, F. F. Chesneau, P. Novák, E. J. Berg, *J. Electrochem. Soc.* **2016**, *163*, A1095.

[226] S.-M. Bak, K.-W. Nam, W. Chang, X. Yu, E. Hu, S. Hwang, E. A. Stach, K.-B. Kim, K. Y. Chung, X.-Q. Yang, *Chem. Mater.* **2013**, *25*, 337.

[227] T. Bartsch, F. Strauss, T. Hatsukade, A. Schiele, A.-Y. Kim, P. Hartmann, J. Janek, T. Brezesinski, *ACS Energy Lett.* **2018**, *3*, 2539.

[228] F. La Mantia, F. Rosciano, N. Tran, P. Novák, *J. Appl. Electrochem.* **2008**, *38*, 893.

[229] S. Hy, F. Felix, J. Rick, W. N. Su, B. J. Hwang, *J. Am. Chem. Soc.* **2014**, *136*, 999.

[230] V. S. Bryantsev, V. Giordani, W. Walker, M. Blanco, S. Zecevic, K. Sasaki, J. Uddin, D. Addison, G. V. Chase, *J. Phys. Chem. A* **2011**, *115*, 12399.

[231] J. Wilcox, S. Patoux, M. Doeff, *J. Electrochem. Soc.* **2009**, *156*, A192.

[232] J. W. Fergus, *J. Power Sources* **2010**, *195*, 939.

[233] K. Min, S.-W. Seo, Y. Y. Song, H. S. Lee, E. Cho, *Phys. Chem. Chem. Phys.* **2017**, *19*, 1762.

[234] F. Zhou, X. Zhao, Z. Lu, J. Jiang, J. R. Dahn, *Electrochem. Commun.* **2008**, *10*, 1168.

[235] L. Croguennec, J. Bains, J. Bréger, C. Tessier, P. Biensan, S. Levasseur, C. Delmas, *J. Electrochem. Soc.* **2011**, *158*, A664.

[236] T. Sasaki, V. Godbole, Y. Takeuchi, Y. Ukyo, P. Novák, *J. Electrochem. Soc.* **2011**, *158*, A1214.

[237] Z. Huang, Z. Wang, X. Zheng, H. Guo, X. Li, Q. Jing, Z. Yang, *Electrochim. Acta* **2015**, *182*, 795.

[238] H. Li, P. Zhou, F. Liu, H. Li, F. Cheng, J. Chen, *Chem. Sci.* **2019**, *10*, 1374.

[239] R. Du, Y. Bi, W. Yang, Z. Peng, M. Liu, Y. Liu, B. Wu, B. Yang, F. Ding, D. Wang, *Ceram. Int.* **2015**, *41*, 7133.

[240] Y. Li, Q. Su, Q. Han, P. Li, L. Li, C. Xu, X. Cao, G. Cao, *Ceram. Int.* **2017**, *43*, 3483.

[241] Z. Yang, W. Xiang, Z. Wu, F. He, J. Zhang, Y. Xiao, B. Zhong, X. Guo, *Ceram. Int.* **2017**, *43*, 3866.

[242] F. Schipper, M. Dixit, D. Kovacheva, M. Talianker, O. Haik, J. Grinblat, E. M. Erickson, C. Ghanty, D. T. Major, B. Markovsky, D. Aurbach, *J. Mater. Chem. A* **2016**, *4*, 16073.

[243] Z. Huang, Z. Wang, Q. Jing, H. Guo, X. Li, Z. Yang, *Electrochim. Acta* **2016**, *192*, 120.

[244] K. Kang, G. Ceder, *Phys. Rev. B* **2006**, *74*, 094105.

[245] X. Li, Z. Xie, W. Liu, W. Ge, H. Wang, M. Qu, *Electrochim. Acta* **2015**, *174*, 1122.

[246] W. Cho, S.-M. Kim, J. H. Song, T. Yim, S.-G. Woo, K.-W. Lee, J.-S. Kim, Y.-J. Kim, *J. Power Sources* **2015**, *282*, 45.

[247] Y. Chen, Y. Zhang, B. Chen, Z. Wang, C. Lu, *J. Power Sources* **2014**, *256*, 20.

[248] D. Wang, X. Li, Z. Wang, H. Guo, Z. Huang, L. Kong, J. Ru, *J. Alloys Compd.* **2015**, *647*, 612.

[249] S. Neudeck, F. Strauss, G. Garcia, H. Wolf, J. Janek, P. Hartmann, T. Brezesinski, *Chem. Commun.* **2019**, *55*, 2174.

[250] Y. Cho, J. Cho, *J. Electrochem. Soc.* **2010**, *157*, A625.

[251] K. Min, C. Jung, D.-S. Ko, K. Kim, J. Jang, K. Park, E. Cho, *ACS Appl. Mater. Interfaces* **2018**, *10*, 20599.

[252] J. Eom, K. Sun Ryu, J. Cho, *J. Electrochem. Soc.* **2008**, *155*, A228.

[253] Y. Kim, J. Cho, *J. Electrochem. Soc.* **2007**, *154*, A495.

[254] H. Lee, Y. Kim, Y.-S. Hong, Y. Kim, M. G. Kim, N.-S. Shin, J. Cho, *J. Electrochem. Soc.* **2006**, *153*, A781.

[255] Z. Wu, S. Ji, T. Liu, Y. Duan, S. Xiao, Y. Lin, K. Xu, F. Pan, *Nano Lett.* **2016**, *16*, 6357.

[256] K. Min, K. Park, S. Y. Park, S.-W. Seo, B. Choi, E. Cho, *Sci. Rep.* **2017**, *7*, 7151.

[257] S. Neudeck, F. Walther, T. Bergfeldt, C. Suchomski, M. Rohnke, P. Hartmann, J. Janek, T. Brezesinski, *ACS Appl. Mater. Interfaces* **2018**, *10*, 20487.

[258] Y.-K. Sun, D.-H. Kim, C. S. Yoon, S.-T. Myung, J. Prakash, K. Amine, *Adv. Funct. Mater.* **2010**, *20*, 485.

[259] Y.-K. Sun, Z. Chen, H.-J. Noh, D.-J. Lee, H.-G. Jung, Y. Ren, S. Wang, C. S. Yoon, S.-T. Myung, K. Amine, *Nat. Mater.* **2012**, *11*, 942.

[260] U.-H. Kim, E.-J. Lee, C. S. Yoon, S.-T. Myung, Y.-K. Sun, *Adv. Energy Mater.* **2016**, *6*, 1601417.

[261] J. H. Lee, C. S. Yoon, J.-Y. Hwang, S.-J. Kim, F. Maglia, P. Lamp, S.-T. Myung, Y.-K. Sun, *Energy Environ. Sci.* **2016**, *9*, 2152.

[262] B.-B. Lim, S.-T. Myung, C. S. Yoon, Y.-K. Sun, *ACS Energy Lett.* **2016**, *1*, 283.

[263] W. Hua, M. Chen, B. Schwarz, M. Knapp, M. Bruns, J. Barthel, X. Yang, F. Sigel, R. Azmi, A. Senyshyn, A. Missiul, L. Simonelli, M. Etter, S. Wang, X. Mu, A. Fiedler, J. R. Binder, X. Guo, S. Chou, B. Zhong, S. Indris, H. Ehrenberg, *Adv. Energy Mater.* **2019**, *9*, 1803094.